Front. Mech. Eng. 2025, 20(1): 8
https://doi.org/10.1007/s11465-025-0824-8

RESEARCH ARTICLE

Liquid film thickness model formed by atomized droplets during sustainable cryogenic air MQL grinding

Mingzheng LIU[a], Changhe LI (✉)[a,b], Qinglong AN[c], Yanbin ZHANG[a], Min YANG[a], Xin CUI[a], Teng GAO[a], Yusuf Suleiman DAMBATTA[a,d], Runze LI[e]

[a] *Key Laboratory of Industrial Fluid Energy Conservation and Pollution Control (Ministry of Education), Qingdao University of Technology, Qingdao 266520, China*
[b] *Qingdao Jimo Qingli Intelligent Manufacturing Industry Research Institute, Qingdao 266201, China*
[c] *School of Mechanical Engineering, Dalian University of Technology, Dalian 116081, China*
[d] *Mechanical Engineering Department, Ahmadu Bello University, Zaria 810106, Nigeria*
[e] *School of Engineering, Department of Biomedical Engineering, Massachusetts Institute of Technology, Boston 02139, USA*

✉ *Corresponding author. Email: sy_lichanghe@163.com (Changhe LI)*

ABSTRACT Surface thermal damage in a difficult-to-process metal precision grinding workpiece has emerged as a technical bottleneck restricting machining quality. As an alternative to traditional pouring cooling, a green clean minimum-quantity lubrication technology still has defects, such as insufficient heat dissipation. The use of cryogenic air instead of normal temperature air, that is, the supply of low-temperature energized lubricant, can effectively improve oil film heat transfer and lubrication performance in a grinding area. Under the premise of ensuring the effective flow of lubricating oil in a grinding zone, the thickness of a liquid film in the wedge zone of a grinding wheel or workpiece is the key factor for determining its performance. However, the dynamic mechanism of droplet formation and distribution of liquid film thickness are still unclear. Hence, the mechanism by which nozzle orientation influences the effective region of a liquid film was analyzed, and the range of nozzle inclination that helps to atomize droplets and enables them to enter the grinding zone was revealed. Then, the dynamic mechanism of atomized droplet film formation was analyzed, and the influence of normal and tangential momentum sources generated by gas impingement perturbation flow and droplet impingement steady flow on the driving effect of liquid film flow was revealed. The thickness distribution model of a liquid film in the impact zone of gas–liquid two-phase flow under different cryogenic air temperatures was established. The model results under different working conditions were obtained by numerical analysis, and validation experiments were carried out. Results show that the measured values agree with the theoretical values. At 0.4 MPa air pressure, the thickness of the liquid film in the impact zone of the atomized droplets increases with decreasing cryogenic air temperature. At −10 and −50 °C, the thickness of the liquid film is 0.92 and 1.26 mm, respectively. Further, on the basis of the surface topography model of cubic boron nitride grinding wheel, the pose relationship of any three adjacent abrasive particles was analyzed, and the theoretical model of abrasive clearance volume was established. The dynamic variation of abrasive clearance volume distribution domain is [70.46, 78.72] mm^3, and the total volume distribution domain is [140.84, 155.67] mm^3. The research will provide a theoretical basis for the application of cryogenic air minimum quantity lubrication technology to hard metal grinding.

KEYWORDS sustainable grinding, cryogenic cooling, minimum quantity lubrication, CAMQL, liquid film thickness, formation mechanism

1 Background

High-end aviation equipment development has focused on achieving lightweight structure, high strength, and high reliability. To meet these requirements, novel metal materials with excellent mechanical properties have been fabricated. However, these materials, typically represented by titanium alloy Ti-6Al-4V, usually have extremely poor processing performance and are thus

Received July 24, 2024; accepted September 19, 2024; online February 20, 2025

called difficult-to-process materials. The processing and manufacturing level of the aviation industry is a key index that reflects the comprehensive strength of a country. The high surface integrity grinding of titanium alloys has become an indispensable method in the field of aerospace. However, in titanium alloy grinding, thermal damage has emerged as the primary technical obstacle. Minimum quantity lubrication is a cleaning technology that has been applied to titanium alloy-assisted grinding but still has some defects, such as insufficient heat dissipation capacity and limited anti-friction ability of lubrication [1]. Cryogenic air can effectively enhance oil film heat conductivity and lubricating capacity in a grinding area and considerably inhibit the negative effects of workpiece surface thermal damage [2].

Cryogenic air minimum quantity lubrication (CAMQL) performs lubrication and cooling by atomizing a lubricant into micron droplets through high-speed and cryogenic air flow. The rapid formation of a thin oil film occurs when atomized droplets come into contact with a workpiece surface and does not flow in a directional way. The oil film is carried into the contact area by a high-speed rotating grinding wheel to lubricate and transfer heat. Meanwhile, a cryogenic oil film plays allows for heat dissipation by enhancing heat transfer [3]. Lubrication or cooling performance hinges on the effective flow of an oil film between a wheel and workpiece [4,5]. When wheel linear velocity and workpiece feed speed are constant, liquid film thickness that forms after atomizing droplets are favorably connected with the effective flowing rate of a lubricant. During lubricant consumption, the thickening of the liquid layer is a crucial element. The key external driving causes of spreading and flowing during thick liquid film formation are the substantial disruption of high-speed air flow and the constant high-frequency impact of droplet groups, leading to a complex liquid film flow process. To date, liquid film formation mechanism and thickness distribution in the grinding process of CAMQL is still unknown. Therefore, studying the film-forming dynamic behavior of atomized droplets is critical to revealing the action mechanism of cryogenic oil films.

A thin liquid film forms when high-speed droplets created by nozzle atomization strike a high-temperature workpiece's surface, and convection, evaporation, and nucleation boiling remove a considerable amount of heat from the surface of the workpiece. Unfortunately, the thickness of formed films has not been measured and examined because of the harsh conditions under spray impact. Martínez-Galván et al. [6] determined the thickness of a liquid film under different levels of pressure for coolant R134a; the results show that dielectric volume flow, surface roughness, and nozzle type have considerable effects on total average film thickness. Pautsch and Shedd [7] used a total internal reflection non-invasive optical technology to examine liquid film thickness after FC-72 spraying; the results show that increasing heat load has no effect on film thickness during single-nozzle atomization. Wu et al. [8] investigated the average thickness of a liquid film created by spraying; the results show that droplet size distribution, impact velocity, and mass flux have direct effects on thickness. Upon reflective fiber sensor's basis, Alekseenko et al. [9] proposed a method for determining the frequency response of liquid film thickness on objects with difficult-to-access position and complex shape; the static, dynamic, and angular characteristics of the sensor are revealed, as well as the measurement results of the film thickness of liquid nitrogen and ethanol aqueous solution flowing down the vertical plate. Using numerical and experimental techniques, Muzik et al. [10] investigated the breaking phenomenon and characteristics of water film flow on the surface of an airfoil. Leng et al. [11,12] used the dispersive confocal displacement meter method to measure the wind-driven flow of a flat plate water film and observed thickness changes at different times at the same position. Cherdantsev et al. [13] concentrated on the stream qualities of a fluid film under high-velocity wind current shearing in level rectangular cylinders in view of laser-actuated fluorescence innovation and proposed various components for fluid film stream to shape layered three-layered structures subjected to wind stream shearing. Chang et al. [14] investigated a water film's thickness and surface wave characteristics. A typical three-dimensional problem is the flow of a flat-water film driven by air flow. Wave shape and dissemination attributes are important features for examining the wave qualities of water films. Using Digital image projection (DIP) technology, Zhang et al. [15] estimated the thickness of a water film on a level surface. Liu et al. [16] investigated variations in water film thickness on a wing driven by air flow. Singh and Tiwari [17] constructed a three-dimensional structure of a liquid film thickness distribution by using a projection grid method. Vinnichenko et al. [18] used a multiple-projection method to measure the deformation of water flow thickness. Hu et al. [19] employed the projection system to observe the transient behavior of a water film and stream on a flat plate under wind power.

However, liquid films formed by nozzle atomization under complex conditions are difficult to directly measure because of limited equipment or technology. Thus, the properties of liquid flow and heat transfer can be revealed by developing a mathematical model to forecast liquid film thickness distribution. Theoretical research on liquid film thickness formed by CAMQL atomization at a workpiece interface is still lacking. Xie et al. [20] developed a mathematical model of spray impact liquid film flow at room temperature, and their findings demonstrate that film thickness calculated theoretically agrees with experimental results obtained at various measurement sites. Assuming a laminar flow for liquid

film flow formed by spray impacting, Mantripragada and Sarkar [21] calculated the liquid film thickness produced by a pressure swirl nozzle; as the experimental film thickness yields a Reynolds number substantially lower than the critical value, film flow is laminar. Cheng et al. [22] developed a theoretical model based on mass-energy conservation that describes the thickness of films in spray cooling. The results show a mass flowing rate-related decrease in film thickness as droplet velocity increases.

In view of the above research status, factors affecting spray film formation mainly include the following aspects: 1) atomization effect, such as air flow temperature, speed, droplet speed, and particle size [23], and 2) the viscosity, density, surface tension, wettability, and other physical characteristics of lubricants. The mechanism of spray film formation is complicated and influenced by many factors and mutual coupling. Consequently, a cryogenic flow liquid film thickness model was established. The dynamic film formation mechanism of atomized droplets with CAMQL was analyzed, and the mechanism for determining effective lubricant flowing rate was examined. The distribution law of clearance volume on a grinding wheel was disclosed through the surface topography of cubic boron nitride (CBN) wheel. The study will provide a theoretical foundation for the use of CAMQL technology in hard metal grinding.

2 Formation mechanism of liquid films

Liquid films created by CAMQL pneumatic atomization is not completely free, in contrast to steady fluid created by a mechanical nozzle's simple pressure atomization. Liquid films are continuously subjected to airflow shearing force and droplet impact force, and input momentum and mass are continuous, and thus liquid films have unstable fluctuating flow [24]. Thin film flow is primarily driven by the momentum created by droplet impact and airflow shearing. Theoretical research published in the literature indicates that the steady flow of droplet impact and the turbulent flow of shearing impact can be superimposed to form a flowing film through CAMQL [25].

(1) Air impingement of disturbed flow. High-speed air flow causes a velocity differential at air–liquid interfaces, causing liquid films to produce interlayer shearing stress from the exterior to the interior along with energy and momentum exchange. Liquid films sink when pressure is higher than its surface tension. Surface waves form when viscous force on the film surface is overcome by shearing force in air–liquid interfaces. The free surfaces of liquid films are unstable and subjected to continuous surface fluctuations under airflow disturbance. Air flow velocity increases, which can cause a decrease in average liquid film thickness and increase in fluctuation frequency.

Normal stress (p_s) and surface shear stress (τ_s) are the primary indicators of air flow's impacts on liquid films. The largest impact effect and flow velocity can be observed at the nozzle axis in an impacting zone. These conditions yield the greatest liquid film flowing rate, largest degree of depression, and lowest liquid film thickness. These properties cause the impact force on the liquid film to gradually decrease with air velocity along the radial direction. Flowing rate decreases gradually, and the liquid film thickens. Outside the impact area of the air flow, only the shearing force of decaying horizontal air flow produces a fluctuating flow.

(2) Droplet impact on steady flow. During steady and uninterrupted atomization, thousands of high-frequency droplet group impacts occur in a unit of time on the liquid film, restricting the assessment of the influence of each droplet. Although the velocity or particle size of each droplet varies, most droplets have little variation in particle size or velocity, and the overall range of change is always contained within a narrow interval. During droplet cluster collision, a dropping liquid film is continuously and uniformly impacted by a droplet cluster, forming a uniformly thick film interface and relatively stable local liquid film thickness [7,26]. Consequently, the influence of droplets on a liquid film in a particular area can be considered a whole during a steady-state and continuous spray procedure. Two typical measures of length are the substrate size R_p and liquid film thickness h_f. Lubrication theory states that given that the thickness is much smaller than the substrate's size, liquid film flow can be simplified (h_f/R_p is approximately 0) [20].

Flow characteristics play a decisive role in the calculation oil film thickness with CAMQL atomization. The impact force of a liquid film per unit area during atomizing film formation is relatively low if droplet particle size is uniform and small, ensuring the uniformity of overall thickness and reducing the number of splashing droplets. The high impact strength of atomized droplets, resulting from an excessive droplet size or velocity, causes a considerable number of droplets to splash out during film formation, impacting flow. Under normal circumstances, the primary effects of droplets are crushing, adhesion, splashing, and rebounding. Droplet–liquid film interaction behavior is highly related to the Weber number *We* and Ohnesorge number *Oh*. The literature has provided a basis for distinguishing droplet motion behavior by observing droplet groups impacting liquid films [27].

$$\begin{cases} We = \dfrac{\rho_d v_d^* D_d}{\sigma_d}, \\ Oh = \dfrac{\mu_d}{\sqrt{\rho_d \sigma_d D_d}}, \\ K = We \cdot Oh^{-0.4}, \end{cases} \tag{1}$$

where ρ_d (kg/m^3) is the density of droplet; v_d* (m/s) is the

normal velocity; D_d (μm) is the size of droplet; σ_d (mN/m) is the tension coefficient of surface; μ_d (N·s/m^2) is the dynamic viscosity; and K is the coefficient of determination.

The characteristics of different phenomena are clearly distinguished, but the influences of secondary parameters are ignored. Based on a substantial body of experimental evidence, Rioboo et al. [28] and Okawa et al. [29] have shown that when the We value is greater than 5 and K value is less than 2100, a liquid film after droplet collision forms a coronal jet and spreads out until fusion without promoting microdroplet splashing. The upper limit of droplet velocity is 12.24 m/s, and the maximum pressure is 0.4 MPa. Table 1 displays a lubricant's viscosity and surface tension at various cryogenic air temperatures. The average particle size of atomized droplets can be calculated as follows [30,31]:

$$D_{ave} = \left[\frac{3\sqrt{2}\pi}{2}\cdot h_l^3\cdot\left(1+\frac{3\mu_l}{\sqrt{\rho_l\sigma_l h_l}}\right)^{1/2}\right]^{1/3}, \quad (2)$$

where μ_l (N·s/m^2) is the kinematic viscosity; σ_l (mN/m) is the tension coefficient of surface; ρ_l (kg/m^3) is the density of liquid film; and h_l (mm) is liquid film thickness at the nozzle, which could be calculated according to Ref. [32].

The CAMQL system and quantitative mapping relationship between physical parameters (temperature, dynamic viscosity, and surface tension coefficient) of a lubricant and cryogenic air temperature are shown in the literature [33]. The dynamic behavior of droplets impacting at various cryogenic air temperatures is ascertained in combination with Eq. (1). Table 1 displays the computation results.

Table 1 also shows that under limiting conditions, the droplet group We values at different cryogenic air temperatures are all greater than 5, and the K values are all less than 2100. Therefore, in theory, droplet group impact liquid films are absorbed after spreading, and droplet splashing does not occur.

2.1 Control equation

A viscose incompressible liquid film flows along a workpiece's surface because of the combined effects of air impact and droplet group liquid film thickness h_f value is much smaller than the λ_f value Boundary layer theory claims that a boundary layer model is what drives a system [34]. Owing to the extremely complex flow of liquid films subjected to external disturbances, reasonable simplification and hypothesis should be made to facilitate analysis: 1) Mass conservation is met when droplets strike a liquid film due to the film's complete absorption of the droplets without any rebounding, splashing, or evaporating. 2) Groups of droplets affect the liquid film's surface uniformly. 3) The vertical momentum becomes the vertical local pressure of liquid film depression, and horizontal component of air flow and droplet momentum becomes the driving force of liquid film horizontal flow within impacting zones [35]. 4) The liquid layer forms a laminar flow on the workpiece's surface and does not slip at the contact interface. 5) Impacts from droplets and air only modify liquid film velocity on a surface. The effects then trickle down through interlayer flow. In a column coordinate system, the liquid film flow control equation is as follows:

(1) Mass conservation equation:

$$\frac{\partial u}{\partial r}+\frac{u}{r}+\frac{\partial w}{\partial z}=0. \quad (3)$$

(2) Momentum conservation equation (r direction):

$$u\frac{\partial u}{\partial r}+w\frac{\partial w}{\partial z}=-\frac{1}{\rho}\frac{\partial p}{\partial r}+\nu\left(\frac{\partial^2 u}{\partial r^2}+\frac{1}{r}\frac{\partial u}{\partial r}-\frac{u}{r^2}+\frac{\partial^2 u}{\partial z^2}\right)+g_r, \quad (4)$$

where g_r (m/s^2) is the unit mass force.

The distance r between an impacting zone and center point is represented by the impacting zone, the range is [0, R_f], and R defines the magnitude of r. z represents the thickness in impacting zone, the range is [0, h_f], and h_f defines the magnitude of z. u represents the flowing rate along r direction in impacting zone, the range is [0, U_f], and U_f defines the magnitude of u. p represents pressure in impacting zone, the range is [0, P_f], and the magnitude of p is defined as P_f. In combination Eq. (3), w represents flowing rate in the direction of z, and the magnitude is $U_f h_f/R_f$. The dimensionless quantities of each variable are

$$u'=\frac{u}{U_f},\ w'=\frac{wR_f}{U_f h_f},\ r'=\frac{r}{R_f},\ z'=\frac{z}{h_f},\ p'=\frac{p}{P_f}. \quad (5)$$

Substituting Eq. (3) into Eq. (4),

Table 1 Droplets impact on liquid film motion behavior determination

Cryogenic air temperature/°C	Air pressure/MPa	Droplet velocity/(m·s^{-1})	Partical size D_{ave}/μm	Dynamic viscosity μ_l/(N·s·m^{-2})	Surface tension coefficient/(mN·m^{-1})	We	Oh	K
−10	0.4	12.24	113.697	102.967	32.123	36.82	1.57	30.74
−20	–	–	124.512	115.865	32.669	39.65	1.67	31.06
−30	–	–	130.365	131.609	33.215	40.83	1.84	31.96
−40	–	–	139.148	151.286	33.761	42.88	2.03	32.28
−50	–	–	148.369	168.854	34.307	44.99	2.18	32.93

$$\frac{U_f h_f^2}{R_f \nu_f}\left(u'\frac{\partial u'}{\partial r'}+w'\frac{\partial u'}{\partial z'}\right)=-\frac{P_f h_f^2}{\rho_f R_f \nu_f U_f}\frac{\partial p'}{\partial r'}+\left[\frac{h_f^2}{R_f^2}\left(\frac{\partial^2 u'}{\partial r'^2}+\frac{1}{r'}\frac{\partial u'}{\partial r'}-\frac{u'}{r'^2}\right)+\frac{\partial^2 u'}{\partial z'^2}\right], \quad (6)$$

where ν_f (m^2/s) is kinematic viscosity and ρ_f (kg/m^3) is density of liquid film.

As reported in Refs. [3,26,36], the order range of each variable in Eq. (6) is 10^{-1} for U_f (m/s), 10^{-2} for R_f (m), 10^{-5}–10^{-4} for h_f (m), 10^5 for P_f (Pa) , 10^{-6} for ν_f (m^2/s) , and 10^{-3} for ρ_f (kg/m^3) . By substituting each corresponding order of magnitude range into Eq. (5), the calculated order of h_f/R_f is much lower than 1, which can be ignored. The $P_f h_f^2/\rho_f R_f \nu_f U_f$ is on the order of slightly less than 1 (approximately 10^{-2}–10^{-1}). According to the simplified hypothesis, flow velocity is derived from air flow and droplet impact and is represented as the momentum equation's velocity term. To calculate the liquid film flow model, this term cannot be disregarded. In Eq. (6), the remaining coefficients can be negligible for the value that is considerably lower than 1. After Eq. (5) is incorporated, the complexity of the conservation of momentum along the r direction can be reduced.

$$-\frac{\partial p}{\partial r}+\mu_f\frac{\partial^2 u}{\partial z^2}+P_r=0, \quad (7)$$

where μ_f ($N\cdot s/m^2$) is dynamic viscosity and P_r ($kg\cdot m^{-2}\cdot s^{-2}$) is momentum source, $P_r=\rho_f\cdot g_r$.

2.2 Boundary conditions

(1) Steady flow with droplets impacting. The horizontal impact force does not change when spray conditions are stable. Velocity difference between liquid film layers cannot be ignored through the viscous force between liquid film layers and lower layers. Flow volume and velocity in the same layer increase concurrently along the r direction because the droplet impact in this direction is constant. Therefore, the continuous transfer of an upper liquid to a lower layer can ensure the mass conservation of a unit body liquid accumulation film.

Surface stability is relatively high for liquid films continuously struck by droplets. A droplet group is fully absorbed by a liquid film changes from being the driving force behind the flow of the liquid film to a physical force or source of momentum inside the film. Two elements of momentum conservation Eq. (7) can describe the momentum-producing source of droplet collision. The impact droplet's axial momentum generates a gradient of local pressure $\partial p/\partial r$, and its radial momentum generates a gradient of shearing stress $\mu_f \partial u/\partial z$, which propels surface flow. The relationship of equilibrium between a viscous force within a liquid layer and the momentum source of an impacting droplet is represented by Eq. (7), as shown in Fig. 1. A droplet at any local liquid film surface in the figure generates momentum, and $P_d = \dot{m}_d \cdot v_d$ and is the source of momentum. $\dot{m}_d$ ($kg\cdot m^{-2}\cdot s^{-1}$) is the droplet local mass flux, and v_d (m/s) is the droplet velocity.

The impact of a droplet group generates shearing force and local pressure on a liquid film, and at a given liquid film position, droplet impact force is assumed to be constant. However, local shearing force and pressure distribution vary as a result of impact force distribution because impact angle changes at different positions [37]. Consequently, droplets at any position $r(i)$ generate tangential and normal momentum sources on a liquid film surface are as follows (Fig. 1):

$$p_{d\_z}=\dot{m}_d v_d \cos\alpha_d=\dot{m}_d v_d\cdot\frac{H_n}{\sqrt{r^2(i)+H_n^2}}, \quad (8)$$

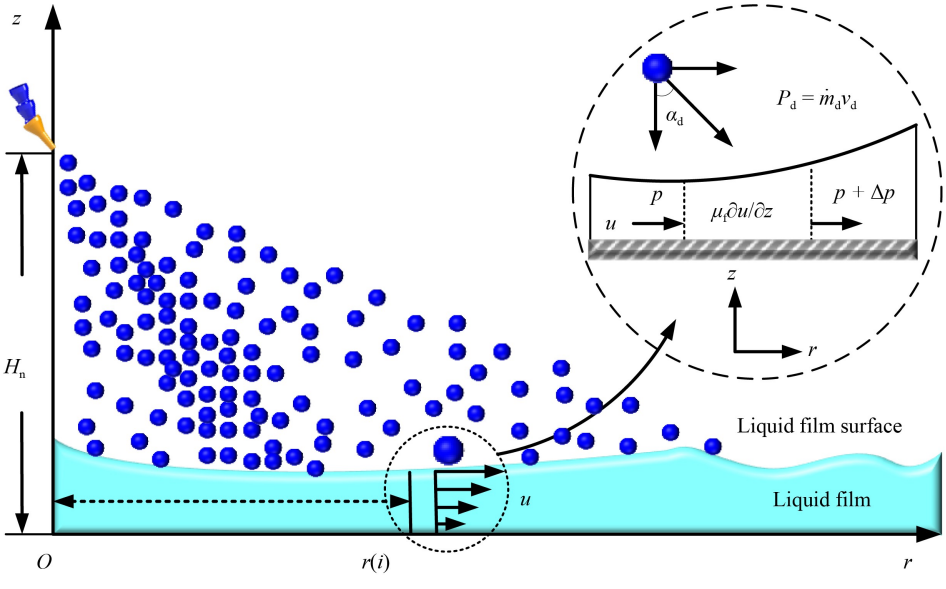

Fig. 1 Relation between droplet momentum source and viscous force of a local liquid film.

$$p_{d\_r} = \dot{m}_d v_d \sin\alpha_d = \dot{m}_d v_d \cdot \frac{r(i)}{\sqrt{r^2(i)+H_n^2}}, \quad (9)$$

where p_{d_z} (kg·m^{-2}·s^{-2}) is the axial momentum source and p_{d_r} (kg·m^{-2}·s^{-2}) is the radial momentum source.

(2) Air impingement of disturbed flow. Currently, pressure distribution within a small stagnation point range can only be measured physically for vertical air impact wall pressure, and measuring the pressure distribution within the entire impact range is challenging, especially for inclined air injection. A useful approach is to examine the connection between wall pressure distribution and jet parameters in an impact range through numerical simulation and mathematical modeling. This section uses modeling and simulation to analyze pressure distribution.

First, the pressure distribution law of vertical air impact wall is analyzed, as shown in Fig. 2. Baydar and Ozmen [38] shows that wall pressure at different spray distances is approximately Gaussian distribution. Nozzle exit pressure and stagnation point pressure are approximately equal when the ratio of nozzle diameter to spray distance is not greater than 8. As spray distance increases, stagnation point pressure decreases, and wall pressure distribution range increases. At an assumed constant injection distance L_n, the half-stagnation point pressure (b_{wp}) is the distance between the position point and stagnation points, and its relationship with injection distance L_n and nozzle diameter D_n is as follows [39]:

$$b_{wp} = -0.016L_n + 0.658D_nL_n^{-1}. \quad (10)$$

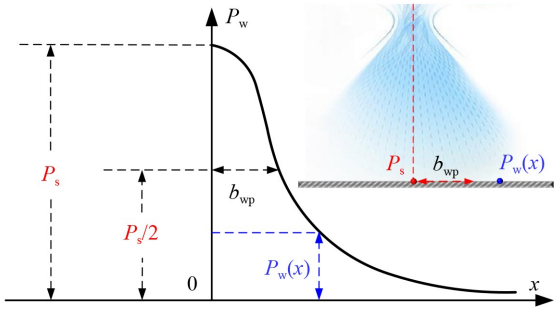

Fig. 2 Vertical flow impact wall pressure distribution.

According to the Gaussian distribution, wall pressure distribution is represented as follows [40]:

$$P_w = P_s \cdot \exp\left(-\frac{0.834x}{b_{wp}}\right), \quad (11)$$

where P_s (MPa) is pressure at stagnation point. P_w (MPa) is the pressure at x, the distance between the stagnation point and wall surface.

The connection between jet distance L_n and stagnation pressure P_s is as follows [39]:

$$P_s = 66.62 \cdot \frac{\rho_a v_a^2 D_n^2}{2L_n^2}. \quad (12)$$

Equation (12) shows that the stagnation pressure P_s exhibits a non-linear change trend and is related to the square of the jet distance L_n in an inverse fashion. However, the distance between the air on both sides of the central axis of the flow and the workpiece surface is considerably asymmetrical for the inclined nozzle injection condition. Consequently, asymmetry is present in the pressure distribution on either side of the stagnation point. In this part, a finite element method is used in examining pressure distribution affecting plates. Airflow at a certain speed v_a passes through the jet distance L_n and impacts on the workpiece wall, gradually reaching a stable state. To guarantee the impact of air disturbance on a wall, the calculation domain measures 300 mm by 60 mm in length. Then, outlet boundary pressure conditions are met. The formula for calculating air velocity at the nozzle exit is

$$v_a = \sqrt{0.024 \cdot V_a \cdot P_{out}}, \quad (13)$$

where V_a (L/min) is air volume at the nozzle and P_{out} (MPa) is the nozzle exit pressure.

Under the quantitative relationship between air volume flow V_a and nozzle exit pressure P_{out}, the distribution trend at nozzle exist flow velocity v_a is shown in Fig. 3. The flow velocity v_a and nozzle exit pressure P_{out} (air volume flowing rate V_a) are approximately positively correlated.

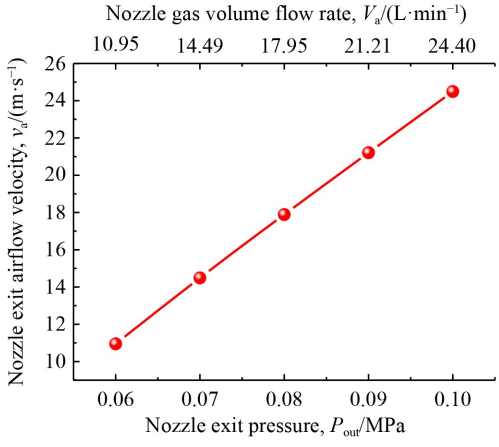

Fig. 3 Flow velocity distribution trend of the nozzle exit.

Taking the nozzle exit flow velocity of 15 m/s as an example. Figure 4 shows that the airflow field created by vertical jet and inclined jet differs considerably. The inclined jet flow field directly turns to form the wall jet after it makes contact with a wall, and no retention area appears, demonstrating strong asymmetry. Consequently, the vertical jet's "stagnation point" is transformed into a "break point" corresponding to an inclined jet. Meanwhile, attenuation amplitude increases with the difference between the speed of a jet and a nozzle. The wall-mounted inclined air jet's pressure distribution is

shown in Fig. 5 at different nozzle exit flow velocities. This figure shows that in the airflow uphill area, wall pressure gradually decreases. In the airflow downhill area, the wall pressure decays quickly. In the downhill zone, the wall pressure is smaller than that in the uphill zone at the same distance from the stagnation point (but not outside its boundaries). The air flow and intensity of the impact on the wall decreases with increasing distance from the downhill area to the contact area, which is relatively small. Subsequently, air flow rapidly shifts to the uphill area after making contact with the wall.

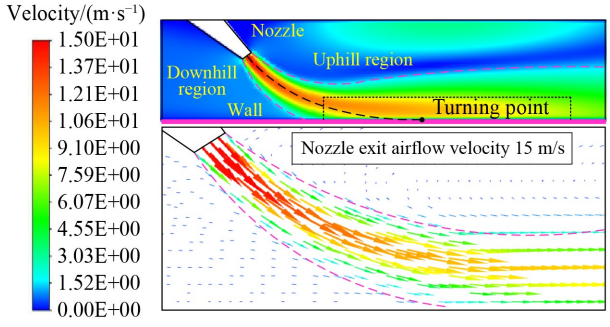

Fig. 4 Impact jet calculation model.

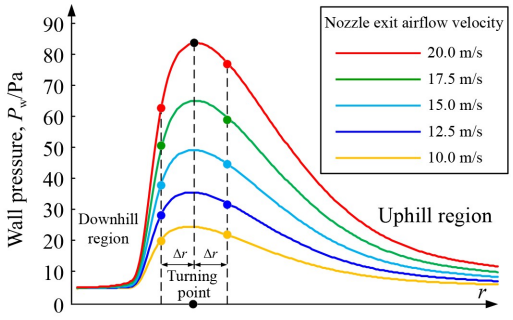

Fig. 5 Pressure distribution of inclined jet impingement plate.

The proportional coefficient β_p is used to describe wall pressure distribution. According to the pressure value distribution on both sides of the break point in Fig. 5, combined with Eq. (11), the corresponding distribution coefficients can be obtained as follows:

$$P'_w = \beta_p \cdot P_w,$$
$$\beta_p = \begin{cases} 1 & \text{Uphill region,} \\ 0.625 & \text{Downhill region,} \end{cases} \tag{14}$$

where P'_w (MPa) is the pressure associated with any position within the impacting zone of inclined airflow.

Impact force in various locations within impacting zone varies. Consequently, tangential stress and normal pressure generated at any given position $r(i)$ on a liquid film respectively are

$$P_{w\_z} = P'_w \cdot \frac{H_n}{\sqrt{r^2(i) + H_n^2}}, \tag{15}$$

$$P_{w\_r} = P'_w \cdot \frac{r(i)}{\sqrt{r^2(i) + H_n^2}}. \tag{16}$$

As shown in Fig. 5, the airflow out of an impacting zone can be considered flowing parallel to the outside surface of a liquid film impacting zone. Air–liquid interfacial shearing force τ_f is a key factor to determining the non-airflow impaction liquid film's thickness [41]. One way to express the interfacial shearing force is using the air–liquid two-phase stratified flow theory [42].

$$\tau_f = f_i \cdot \frac{1}{2}\rho_a (v'_a - C_f), \tag{17}$$

where f_i is the shearing coefficient; ρ_a (kg/m^3) is the air density; v'_a (m/s) is horizontal airflow velocity; and C_f (m/s) is the interface wave's phase velocity between liquid and air, which is well below the airflow velocity v'_a and hence can be disregarded [43].

The frequency of fluctuations in a liquid film surface increases with airflow Reynolds number when airflow velocity and thickness change. This change shows that liquid film surface fluctuation behavior is primarily influenced by high velocity air flow. Surface tension and gravity prevent interfacial fluctuation when air–liquid velocity difference is minimal. An unstable interface condition worsens as velocity differential increases. Through energy exchange, a liquid film accelerates until it overcomes its own viscous force and begins to fluctuate. The findings demonstrate that in the presence of low velocity airflow, shearing force at an air–liquid interface is approximately equal to friction stress between a liquid film and wall. Based on this relationship, the plate boundary layer model is used in approximating interface shearing coefficient f_i [44,45].

$$f_i = 0.074 \cdot Re_a^{-0.2}, \tag{18}$$

where Re_a is the airflow Reynolds number, $Re_a = v'_a L_a/\mu_a$, and $v'_a = v_a \cdot \tan(\theta_s/2)$. L_a is the horizontal airflow thickness, and $L_a = 3$ mm according to simulation results.

2.3 Model establishment

(1) Inside impacting zone. In conjunction with Eq. (7) and the mechanical behavior of gas-liquid mixed flow, total momentum source P_r throughout the surface layer's horizontal direction is:

$$P_r = P_{d\_r} + \frac{\partial P_{w\_r}}{\partial r}. \tag{19}$$

The shearing stress τ_{total} and pressure P_{total} of the air–liquid contact interface are:

$$\begin{cases} \tau_{total} = P_{w\_r} + P_{d\_r} \cdot w, \\ P_{total} = P_{w\_z} + P_{d\_z} \cdot w. \end{cases} \tag{20}$$

Combining Eqs. (7), (19), and (20) can yield the flowing velocity inside the liquid film at any height z and position r:

$$u(r)_{\_\text{in}} = \frac{z}{\mu_\text{f}}\left[\tau_\text{total} + P_r \cdot h_\text{f}(r) - \frac{\partial P_\text{total}}{\partial r} \cdot h_\text{f}(r)\right] - \frac{z^2}{2\mu_\text{f}}\left[P_r \cdot h_\text{f}(r) - \frac{\partial P_\text{total}}{\partial r}\right]. \quad (21)$$

According to Eq. (21), in relation to the wheel width w, the liquid film flow Q_f is

$$Q_\text{f} = w \cdot \rho_\text{f} \int_0^{h_\text{f}(r)} u(r)_{\_\text{in}} \text{d}z = \frac{w \cdot \rho_\text{f}}{\mu_\text{f}}\left(\frac{\tau_\text{total} \cdot h_\text{f}(r)^2}{2} + \frac{(P_r - \partial P_\text{total}/\partial r) \cdot h_\text{f}(r)^3}{3}\right). \quad (22)$$

The design of a platform for measuring lubricant flow through the width of a grinding wheel is based on the CAMQL system. The contact point should be gap free as soon as the drainage plate is secured to the workpiece's horizontal surface. To prevent measurement errors due to overspreading on the drainage plate, the plate's height should surpass the liquid film's thickness. An equal width difference between the front drainage plate and grinding wheel appears. After the CAMQL device is started, when liquid film flow is stable at various low temperatures, the end of the drainage plate is placed into the measuring cylinder to collect the lubricant. To ensure that the oil film flows completely and measurement error is reduced, a 10 s collection time is used.

After data collection and measurement, Eq. (22) can be incorporated to obtain the distribution law of thickness at various cryogenic air temperatures, as shown in Fig. 6. The Q_f value is related to the grinding wheel width w and exhibits a decreasing trend as the cryogenic air temperature drops. A decrease in cryogenic air temperature causes the lubricant's viscosity to increase exponentially. The degree of flowing obstruction is greatly increased while the interlayer viscous force and friction between the workpiece surface and liquid film increase simultaneously. Therefore, the amount of lubricants passed per unit width is reduced. At different cryogenic air temperatures, along the radial characteristic points, the h_f value first decreases and then increases from −3 to 7 mm in the spray impacting zone. The minimum value of h_f is obtained at the impact center of air–liquid two-phase flow. The reason behind this is that at the impact center, in comparison with other characteristic points, the air–liquid two-phase flow exhibits relatively high impact strength, impact velocity, and droplet group density. In addition to the liquid film's relatively quick flow, tangential stress and normal pressure reach their maximum values. Thus, the minimum thickness is obtained. In other positions, the gas–liquid impact force is weakened, and flow speed decreases. The amount of liquid per unit time is reduced at the corresponding position. The thickness increases gradually as a result of the liquid film's constant replenishment and accumulation. In addition, the mechanism of low temperature influence on flow is similar to the spray impacting zone, where thickness increases at different characteristic positions as the cryogenic air temperature decreases impacting zone. The spreading area and liquid film fluidity both decrease with decreasing lubricant temperature. Consequently, the thicker the liquid film, assuming a given oil film volume.

(2) Outside the impacting zone of air–liquid two-phase flow. Outside the air–liquid jet region, only horizontal air flow affects a flowing liquid film. Horizontal flow is considered to only cause shearing force on liquid film because of its extremely short acting distance. At a liquid–solid–air interface, the continuous interfacial

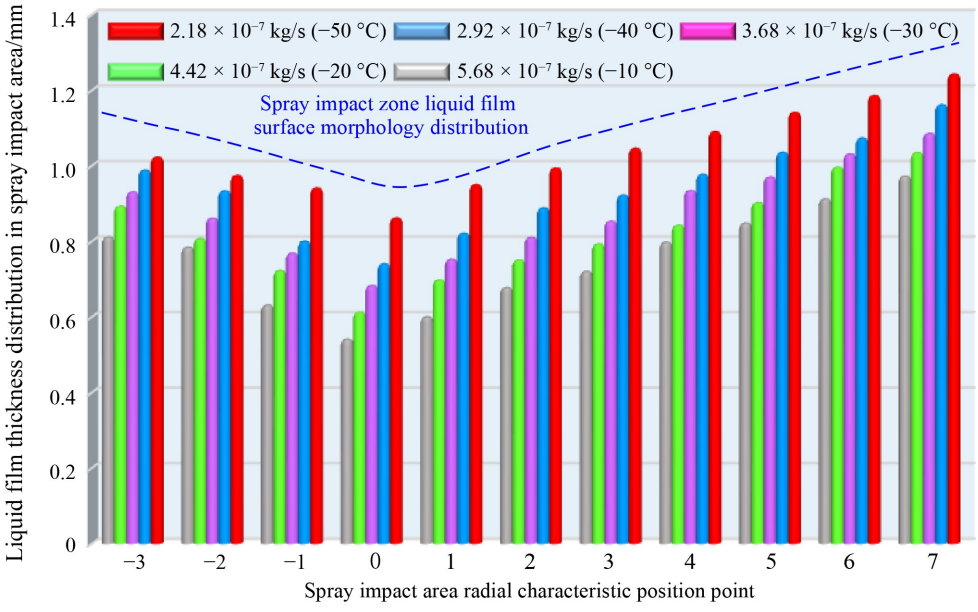

Fig. 6 Liquid film thickness distribution in jet zone at different cryogenic air temperature.

shearing stress/pressure and interfacial layer without slipping are satisfied. By integrating the simplified Eq. (7) of the momentum conservation equation:

$$u(r)_{\_out} = \frac{1}{2\mu_f}\frac{\partial P_{out\_a}}{\partial r}\cdot r^2 + \frac{\tau_f}{\mu_f}\cdot r, \tag{23}$$

where τ_f (MPa) is interfacial shearing stress outside the impacting region. P_{out_a} (MPa) is the air flow pressure.

Under the assumed conditions, if air flow does not change the liquid film pressure, then $\partial P_{out}/\partial r$ is approximately 0. By integrating Eq. (23) along the liquid film thickness direction, the following method will yield the flowing rate:

$$Q_f = \rho_f \cdot w \cdot \int_0^{h_f(r)} u(r)_{\_out}\,dz = \rho_f \cdot w \cdot \frac{\tau_f}{2\mu_f}\cdot h_f^2(r). \tag{24}$$

In combination with Eqs. (23) and (24), the liquid film thickness outside the impacting zone is

$$h_f(r) = \sqrt{\frac{2\mu_f Q_f \rho_f w}{0.037\rho_a v_a' Re_a^{-0.2}}}. \tag{25}$$

Thickness distribution outside the impacting zone at various cryogenic air temperatures is shown in Fig. 7. Viscosity is relatively larger due to the cryogenic environment. As the air temperature drops, thickness exhibits an increasing trend. This is a result of the liquid film flowing in an irregular manner brought on by air movement. In theory, thickness at crest is the same as that at impacting zone edge, but the thickness decreases at the trough. Thickness obtained by Eq. (25) is the equivalent average value, so the value decreases in comparison.

3 Measurement of film thickness

Based on the modest data processing volume and straightforward image processing technique, the DIP method can clearly and accurately display three-dimensional morphology [46].

3.1 Experimental platform

Figure 8 illustrates the general idea of measuring thickness with the DIP technology. The reference plane in the z direction is assumed to have a height of 0. From the perspective of a projector, when no liquid flow occurs on the substrate, any mesh intersection is projected at point A. The rays from the initial projection point A are refracted at surface D, thus projecting at point C, when a specific amount of liquid is passing through the substrate's projection region. The initial projection point A is moved to point C from the camera's point of view. Thus, the displacement is indicated by the distance $|CA|$. The horizontal distance between camera and projector is d_p. Vertical distance is s_p. ΔMND and ΔCAD can be analyzed geometrically as follows:

$$\frac{d_p}{|CA|} = \frac{s_p - |BD|}{|BD|}. \tag{26}$$

The formula above can be simplified as follows because the distance s_p is significantly greater than $|BD|$.

$$|BD| = \frac{s_p}{d_p}\cdot|CA| = K_p\cdot|CA|. \tag{27}$$

For the adjusted experimental measurement system, s_p and d_p have set values. Consequently, K_p is a constant parameter that can be found using a calibration technique. Equation (27) shows that the liquid film thickness $|BD|$ and image offset $|CA|$ possess a linear connection. The $|BD|$ value can be calculated, and a three-dimensional representation of the entire region in real time can be created by obtaining the $|CA|$ value of an image offset.

The fundamental technique for calculating image offset

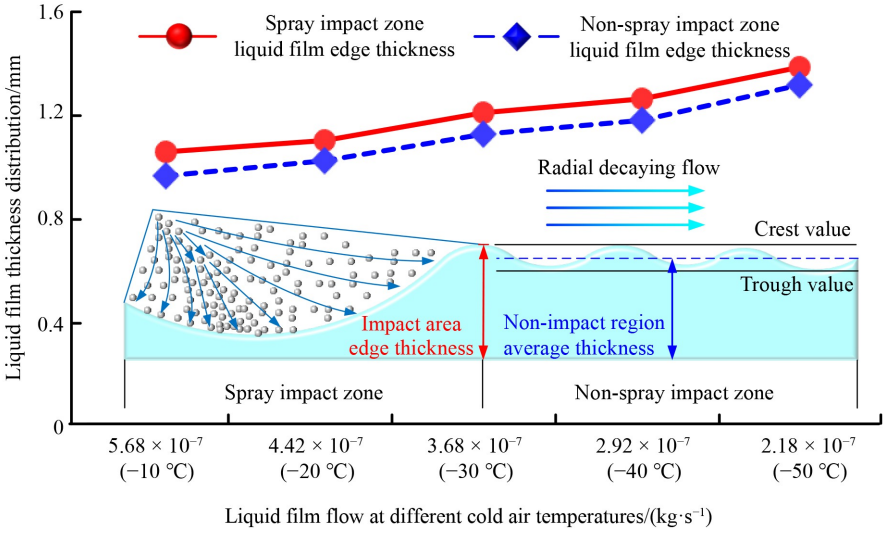

Fig. 7 Liquid film thickness distribution out jet zone at different cryogenic air temperatures.

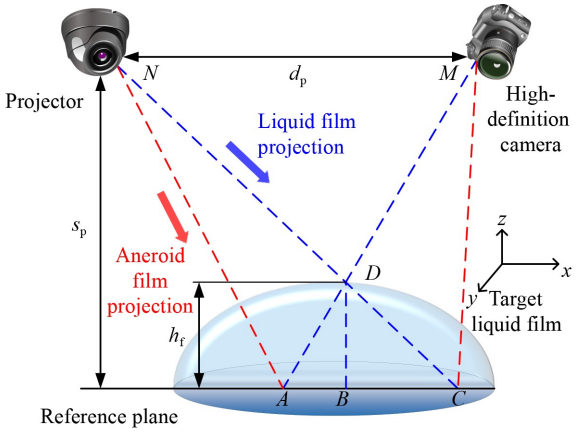

Fig. 8 Principle of measuring liquid film thickness with an image projection technology.

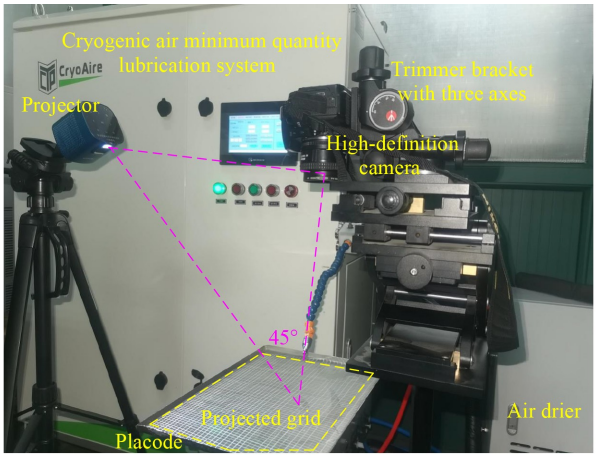

Fig. 9 Cryogenic liquid film measurement experimental platform.

is the image cross-correlation algorithm [47]. Projection points are distributed in a single area by partitioning reference or measured images synchronously according to a certain size. All segmented images are numbered and associated in accordance with the mapping principle. The image cross-correlation algorithm computes the correlation coefficient of each association combination. Through ascertaining correlation coefficient's peak position, the offset of two correlation combinations can be determined, that is, the focus displacement. When the grid in the migration region covers the liquid film with a difference in thickness, different grid nodes have different size offset along the projection direction compared with the benchmark grid. According to the mesh size, synchronous regionalization segmentation is carried out to ensure that the two images' matching grid nodes are located in the corresponding micro-region, and the displacement of the grid points in the red box can be obtained by using the above algorithm.

Based on the CAMQL equipment, the measurement experiment platform is built, as shown in Fig. 9. The primary element that enhances measurement accuracy is image resolution. The high-definition camera used has a resolution of 2.1 × 10^7 pixels and shooting area of 120 mm × 140 mm. A high-precision projector is used to project a single 2 mm × 2 mm grid. The camera, substrate, and projector are arranged in a triangle, and the lens of the projector and camera should be at the same level. A specific angle is tilted in the projector lens. Then, the camera orientation should be perpendicular to the substrate. The focus of the grid intersection points should be high. This step prevents the grid from being distorted by excessive tilt angle. After multiple debugging cycles are completed, the camera and projector are positioned at 45° vertical angle. The cooling medium is supplied with an integrated CryoAire CEA361 CAMQL system, and −60 °C is the lowest cooling temperature, detailed in the previous research literature [3]. To transfer cryogenic air and minimize heat loss, the nozzle, which is a part of the internal mixing structure, uses a special material pipe.

3.2 Calibration method

Regarding a test setup where the camera and projector are fixed, the offset of grid points in the matching areas of the reference or measurement images is directly correlated with the vertical substrate height. The K_p value is determined through calibration. Figure 10(a) depicts the calibration system. The projector and camera are still in their original positions. The substrate is fixed horizontally on top of a three-axis lift platform powered at the micron-scale. The lifting platform's height is adjusted 500 μm from the reference plane during calibration. The platform maintains its various z-axis positions. The associated position's grid image is obtained by the camera, stored in the computer, and segmented. Then, the offset of interconnection combination can be calculated. Referring to the image located at z = 0, the target grid offset points at different positions of the substrate is calculated. Figure 10(b) shows the change rule of pixel displacement and corresponding lifting height of target grid points in the selected segmentation image. Figure 10(b) shows that L_p and N_p show a linear relationship. The change rate is K_p.

3.3 Measurement results

To better record the transient characteristics, the camera records the image at a frame rate of 30 fps. Based on necessary conditions for the effective area in the wedge zone, the thickness in the effective area at various air temperatures is measured using the DIP system (Fig. 11). Variations in cryogenic settings result in notable changes in the spreading morphology of the liquid films. The lower the cryogenic air temperature is, the smaller the spread area of a liquid film is and the more irregular the shape is. At −10 °C, the liquid film spreads widely, almost covering the set rectangular area, and the shape is similar to that of a rectangle. The lubricant's viscosity rises as cryogenic air temperature drops, and liquid film is

prevented from spreading by the interlayer viscous force of the oil itself. Owing to the non-uniformity of the external driving force of an actual liquid film, flow velocity at different positions considerably varies, and thus edge morphology tends to be an irregular evolution process. In the impact area of air–liquid two-phase flow, thickness gradually increases from low to high from the center to the outside. From the cloud image, it is visible on the right of Fig. 11 that under different cryogenic conditions, the liquid film thickness presents an approximate symmetric distribution along the jet direction. This reflects from the side that the atomizing jet of CAMQL is comparatively stable.

The precision of the liquid film model for cryogenic flow is verified by selecting calculation points that correspond to the theoretical analysis in the impacting zone and non-impacting zone of the actual liquid film. Thickness values are read at corresponding positions. The experimental and theoretical thickness values at low temperatures are compared (Fig. 12). This figure illustrates that at different cryogenic air temperatures, the theoretically calculated and experimentally measured values follow a largely consistent variation trend along the sampling points, but the experimental values are smaller than the theoretical values because of accumulated measurement bias caused by various factors in the course of the experiment. The following is an analysis of the error sources: 1) The grid lines on the substrate are distorted to a certain extent when the grid is projected at a specific angle by the projector, and the cross-region distribution of grid intersections may occur when the program is regionalized. 2) Theoretically, the more accurate the calculations and the smoother the image are, the smaller the projected mesh size and the higher the density are after the final program identification. However, if the grid density is extremely large in the actual projection, the camera's clarity will decrease, and recognition errors will result from the grid's density.

4 Effective lubricant flow

During grinding, high-speed or pressure impact causes grinding fluid "side leakage". A full liquid film formation by the lubricant is hampered as a result [48]. The presence or absence of a boundary lubricating film during grinding is directly influenced by the amount of lubricant between friction pairs. The wheel–workpiece contact area is nearly closed. When the oil level is low, the adsorption number of active molecules is relatively low, and a thin lubrication film forms. Oil film thickness increases with oil content, forming a stable adsorption film. The workpiece surface with a particular roughness has micro-grooves where extra lubricant is collected. The lubricant will reach the peak and fill the area's groove once the oil volume is completely composed of the lubricant. The grinding zone cannot be adequately lubricated if the flow of oil into it is extremely low. A proper supply of lubricants for bearing and lubrication needs to be provided to the grinding zone to meet the effective utilization rate of the lubricant. Therefore, investigating how the effective flowing rate lubricant is impacted by abrasive clearance volume is imperative.

4.1 Surface topography

Research shows that CBN wheel is suitable for Ti-6Al-4V grinding [49–51]. Therefore, this study selects a CBN grinding wheel (80#) for theoretical and experimental research. Currently, abrasive particles are primarily spherical or conical in the recognized model [52]. The surface morphology of the CBN wheel is observed with a microscope. Abrasive particles are irregular edge bodies, and the short sliding and plowing stages of edge body wear occur during grinding. As a result, the buildup of plastic material is reduced along the cutting path's border and facilitates the formation of an enhanced machining surface [53]. Therefore, to facilitate calculation and

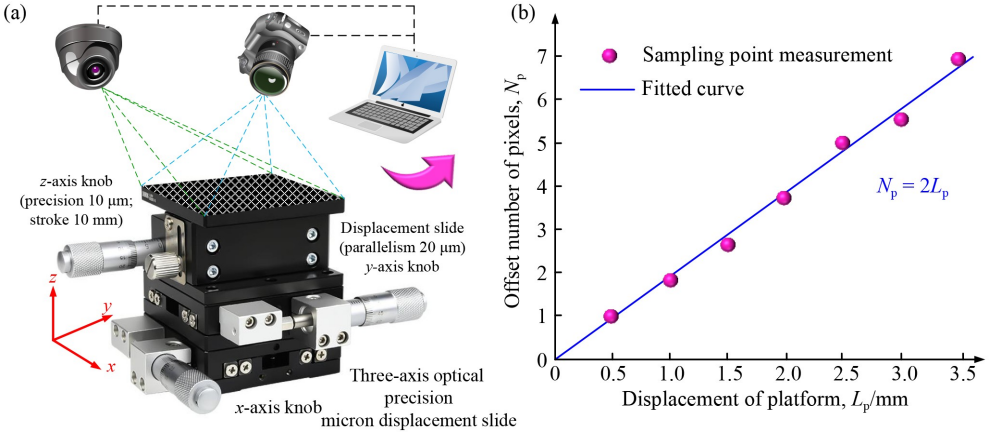

Fig. 10 DIP platform calibration and result. (a) Calibration system. (b) Change rule of pixel displacement and corresponding lifting height of target grid points.

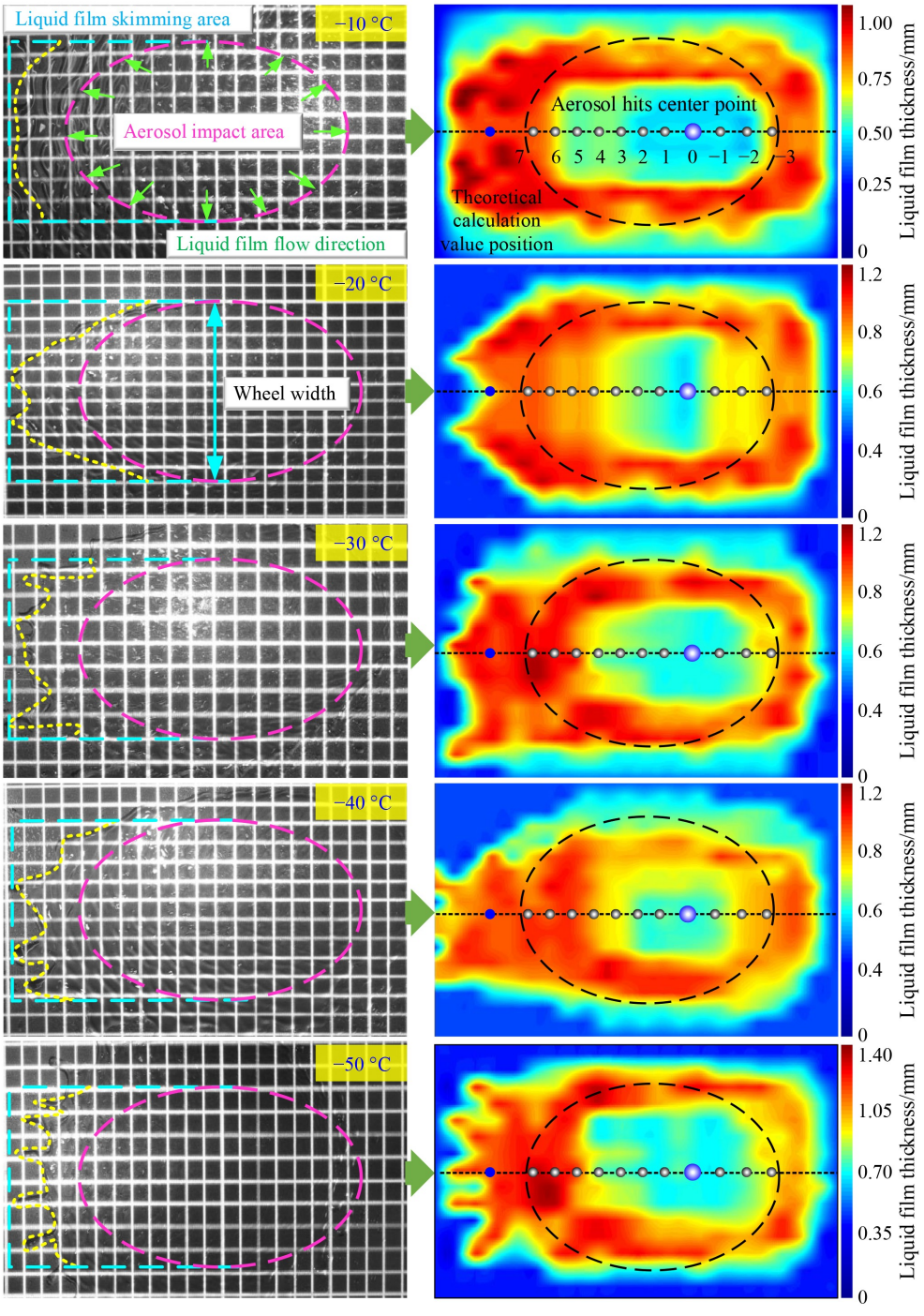

Fig. 11 Distribution of effective area liquid film thickness at different low temperatures.

analysis, a regular tetra pyramidal shape is thought to be the form of the wear particle.

According to Refs. [49,54–56], the particle size $D^{(i)}$, vertex angle $\alpha^{(i)}$, particle rotation angle around the three coordinate axes ($\Delta\theta_x$, $\Delta\theta_y$, $\Delta\theta_z$), and protrusive height $h^{(i)}$ of any abrasive particle i are determined. The bottom surface central coordinates of abrasive particle are set as ($x^{(i)}$, $y^{(i)}$, $z^{(i)}$), the abrasive particle vibration method [57] is adopted, and the model of surface topography is represented as matrix $\boldsymbol{G_N}$.

$$\boldsymbol{G}_N = \begin{bmatrix} x_{\_1}^{(i)} & y_{\_1}^{(i)} & z_{\_1}^{(i)} & d_{\_1}^{(i)} & h_{\_1}^{(i)} & \alpha_{\_1}^{(i)} & \Delta\theta_{x\_1}^{(i)} & \Delta\theta_{y\_1}^{(i)} & \Delta\theta_{z\_1}^{(i)} \\ x_{\_2}^{(i)} & y_{\_2}^{(i)} & z_{\_2}^{(i)} & d_{\_2}^{(i)} & h_{\_2}^{(i)} & \alpha_{\_2}^{(i)} & \Delta\theta_{x\_2}^{(i)} & \Delta\theta_{y\_2}^{(i)} & \Delta\theta_{z\_2}^{(i)} \\ \vdots & \vdots & \vdots & \vdots & \vdots & \vdots & \vdots & \vdots & \vdots \\ x_{\_N}^{(i)} & y_{\_N}^{(i)} & z_{\_N}^{(i)} & d_{\_N}^{(i)} & h_{\_N}^{(i)} & \alpha_{\_N}^{(i)} & \Delta\theta_{x\_N}^{(i)} & \Delta\theta_{y\_N}^{(i)} & \Delta\theta_{z\_N}^{(i)} \end{bmatrix}. \tag{28}$$

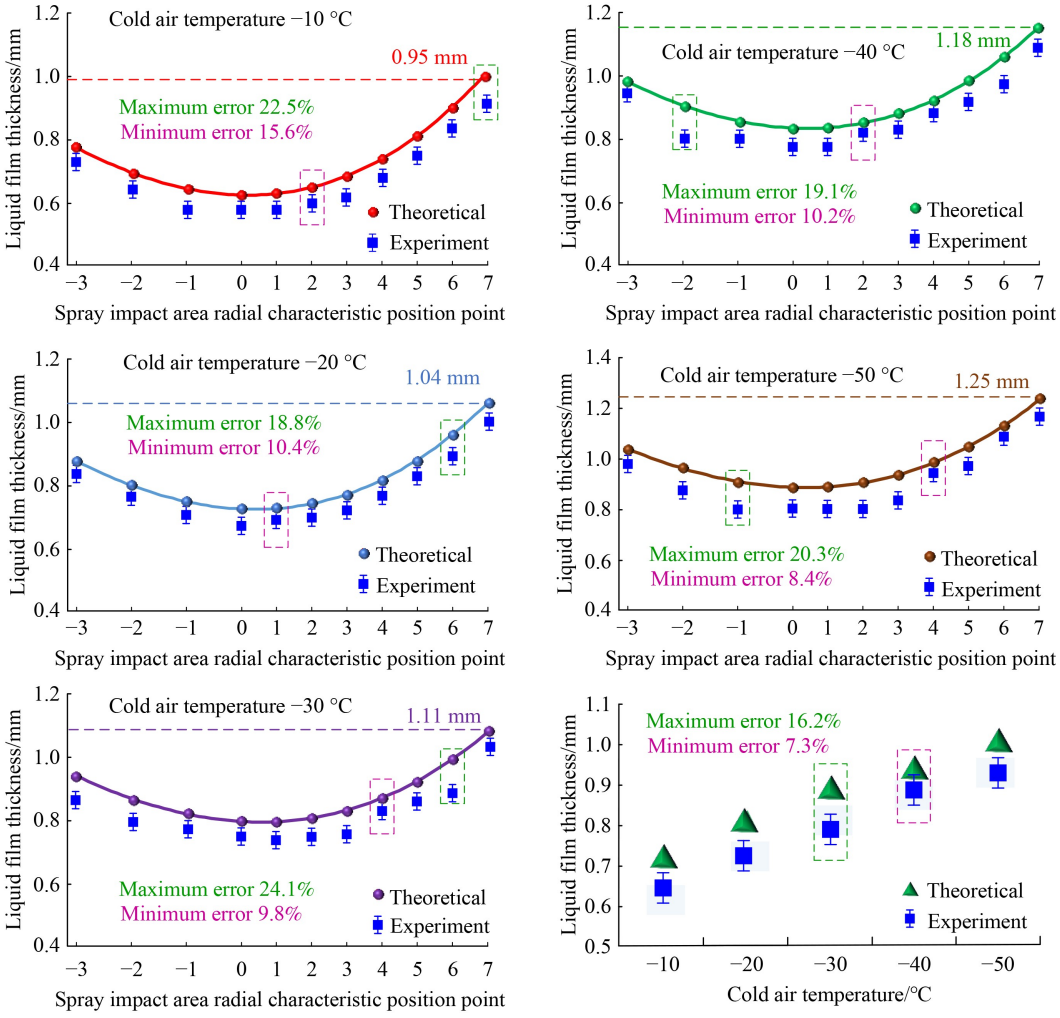

Fig. 12 Comparison between theoretical and experimental values of liquid film thickness.

Surface topography is displayed in Fig. 13 after programming simulation.

4.2 Clearance volume

Abrasive clearance directly determines the effective flowing rate of a lubricant. The amount of a lubricant that can be accommodated increases with abrasive clearance. However, effective abrasive particles per unit area are few due to the high abrasive clearance, which decreases a grinding wheel's strength to some degree and leads to a reduction in cutting performance. For titanium alloys, high levels of friction can quickly shorten wheel life and decrease grinding accuracy. Therefore, grinding performance is greatly influenced by grain clearance size. Grinding parameters are found to have little effect on effective flowing rate, and the main variables influencing effective flowing rate are abrasive clearance, nozzle orientation, and lubricant physical properties [58]. After the volume of the abrasive clearance space is determined, a grinding wheel's lubricant capacity per unit of time can be estimated.

According to the surface topography model in [56], before the abrasive clearance space volume model can be established, the following presumptions need to be made: 1) The surface of the binder is set to the base surface and smooth laying, and the effect of roughness on volume is ignored. 2) Abrasive particles are all tetra pyramidal and perpendicular to the surface of the binder, that is, the two degrees of freedom rotation of the abrasive space is ignored, and only the dimensional rotation of the abrasive particles around the normal surface of the binder is retained. 3) The average parameters of all abrasive particles in the grinding zone are calculated. 4) A straight line cannot contain any three nearby abrasive particle. 5) Abrasive wear is ignored. 6) No blockage is present in the abrasive gap.

Under the above assumed conditions, the geometry and position distribution of three adjacent abrasive particles are shown in Fig. 14. A system of coordinates in three dimensions is created, and ΔABC is projected as $\Delta A'B'C'$ on the base plane. According to the setting mechanism of abrasive position on wheel surface in [56], the projection

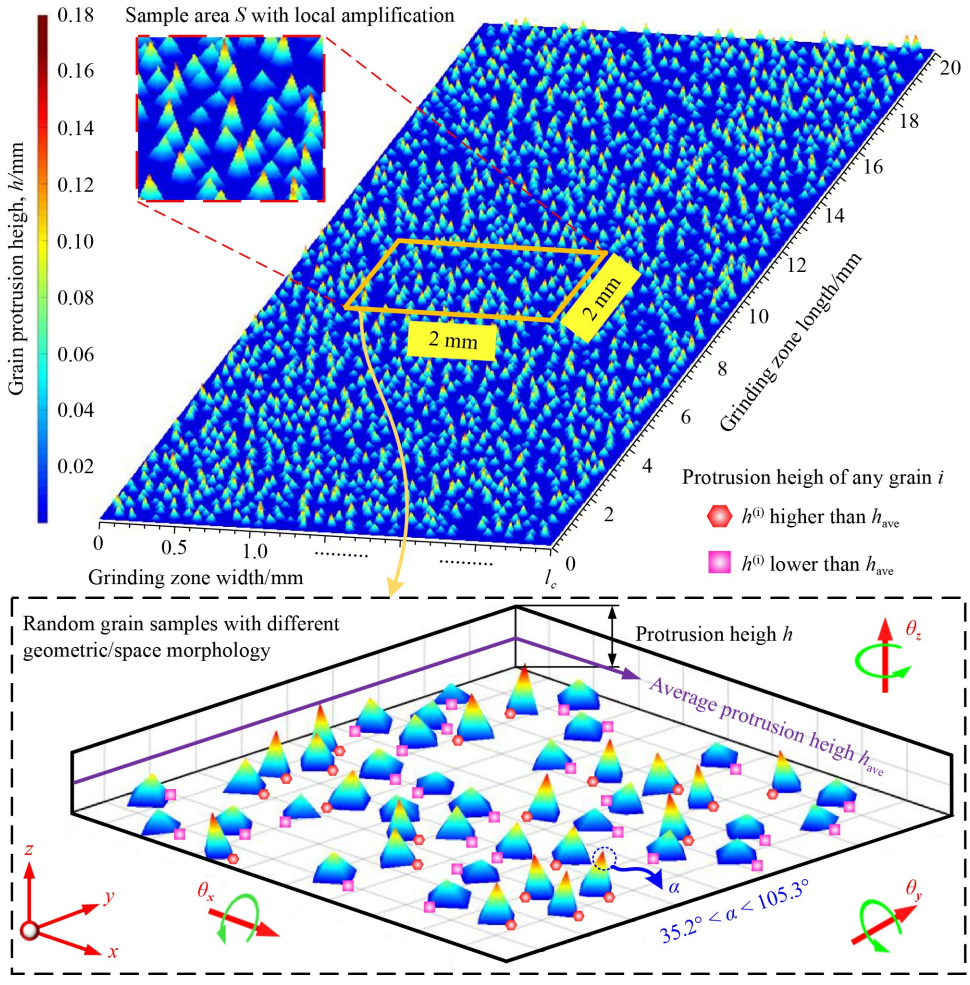

Fig. 13 CBN grinding wheel surface topography based on the random distribution of the grain [59].

of abrasive particle vertex A, B, and C correspond to the positioning coordinates of the three abrasive particles. Thus, the vertex of the particle and the projection point correspond to each other and form a triangular prism. Owing to variations in height at which wear grains protrude, the top surface of the triangular prism has a certain inclination to the horizontal plane. Thus, the irregularity of the triangular prism cannot be calculated directly. The computation procedure is simplified by averaging the protrusive heights ($h_{\mathrm{a}}^{(i)}$, $h_{\mathrm{b}}^{(i)}$, and $h_{\mathrm{c}}^{(i)}$) of the three abrasive particles. As a positive triangular prism, the original irregular prism can be represented by the following volume formula:

$$V_n^{(i)} = \frac{h_{\mathrm{a}}^{(i)} + h_{\mathrm{b}}^{(i)} + h_{\mathrm{c}}^{(i)}}{3} \cdot S_{\Delta A'B'C'}, \tag{29}$$

where $S_{\Delta A'B'C'}$ (mm^2) is the projected triangle's area.

$S_{\Delta A'B'C'}$ can be expressed by

$$S_{\Delta A'B'C'} = \left[P_{\mathrm{t}} \cdot (P_{\mathrm{t}} - l_{(i,j)\text{-}(i,j+1)}) \cdot (P_{\mathrm{t}} - l_{(i,j)\text{-}(i+1,j)}) \cdot (P_{\mathrm{t}} - l_{(i+1,j)\text{-}(i,j+1)})\right]^{1/2}, \tag{30}$$

where l (μm) is any side of $S_{\Delta A'B'C'}$ and P_{t} (mm) is the half circumference of $S_{\Delta A'B'C'}$.

$$P_{\mathrm{t}} = \frac{l_{(i,j)\text{-}(i,j+1)} + l_{(i,j)\text{-}(i+1,j)} + l_{(i+1,j)\text{-}(i,j+1)}}{2}. \tag{31}$$

According to the projection point's coordinates, the three side lengths can be obtained as follows:

$$\begin{cases} l_{(i,j)\text{-}(i,j+1)} = \sqrt{(x_{i,j} - x_{i,j+1})^2 + (y_{i,j} - y_{i,j+1})^2} & (AB), \\ l_{(i,j)\text{-}(i+1,j)} = \sqrt{(x_{i,j} - x_{i+1,j})^2 + (y_{i,j} - y_{i+1,j})^2} & (AC), \\ l_{(i+1,j)\text{-}(i,j+1)} = \sqrt{(x_{i+1,j} - x_{i,j+1})^2 + (y_{i+1,j} - y_{i,j+1})^2} & (BC). \end{cases} \tag{32}$$

Nonetheless, the three abrasive particles are somewhat disrupted by the triangle prism. Therefore, the volumes ($V_{\mathrm{a}}^{(i)}$, $V_{\mathrm{b}}^{(i)}$, and $V_{\mathrm{c}}^{(i)}$) of the three interference parts need to be removed, and the interference part is shown in Fig. 14. Based on assumption 2, the abrasive particles rotate at an arbitrary angle around the z-axis. However, no matter how the abrasive particle rotates, any interference part has a projected area that is greater than zero and less than half of the corresponding abrasive bottom area. Given that the vertex angle of each particle is different, the bottom area

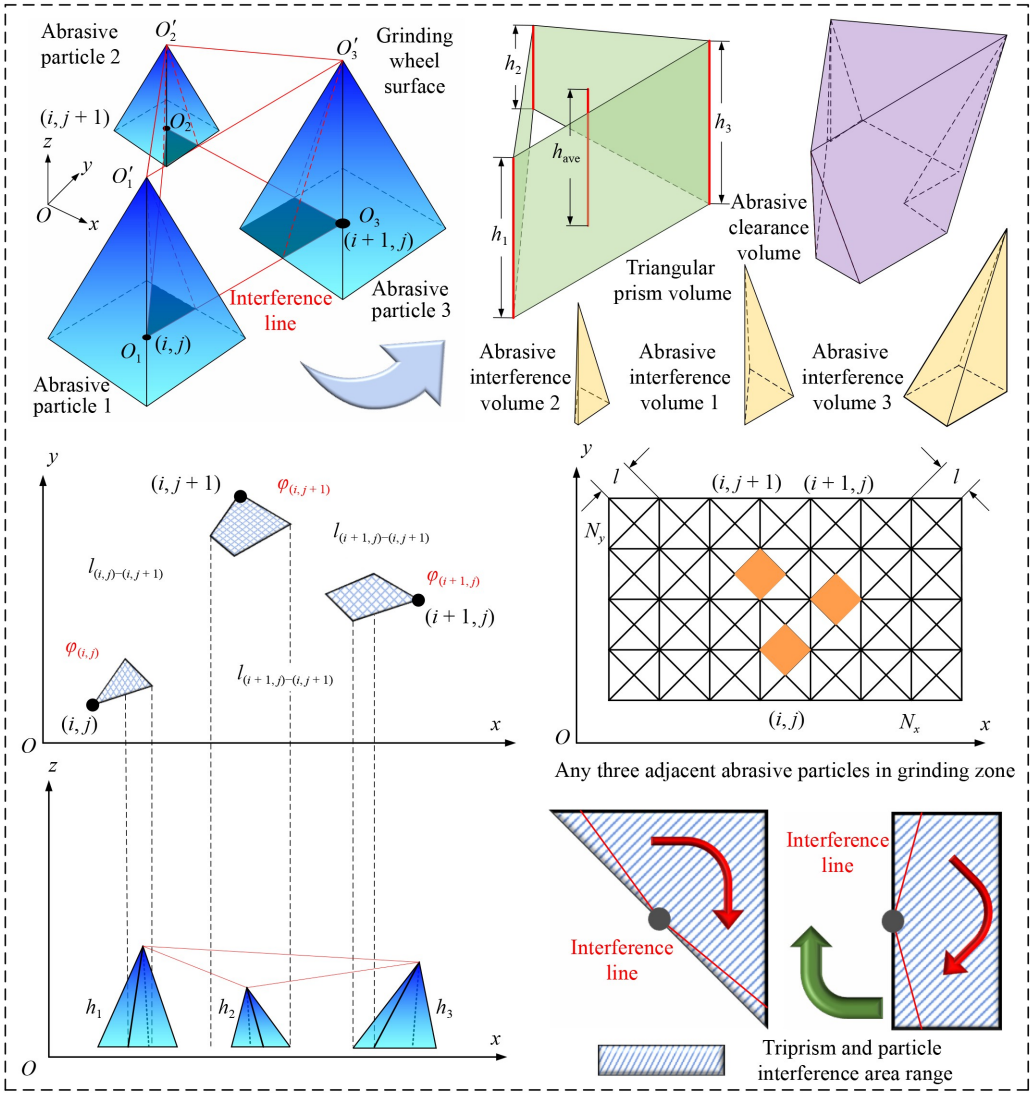

Fig. 14 Space volume model of three adjacent abrasive grains on the grinding wheel surface.

of the particle is evidently different. In addition, the arbitrary rotation of the abrasive particle around the z-axis makes the projected area impossible to be obtained. The projected area $S_{\mathrm{t}}^{(i)}$ of the corresponding interference part is positively correlated with the projected angle $\varphi_{\mathrm{p}}^{(i)}$. Therefore, the projected area of the interference part can be calculated by assuming that the proportion of the projected area $S_{\mathrm{t}}^{(i)}$ to half of the abrasive bottom area $S_{\mathrm{d}}^{(i)}$ is equal to the ratio of the corresponding projected angle to 180°, that is,

$$\frac{S_{\mathrm{t}}^{(i)}}{0.5\cdot S_{\mathrm{d}}^{(i)}}=\frac{\varphi_{\mathrm{p}}^{(i)}}{180^{\circ}}. \tag{33}$$

The corresponding projection angle can be obtained as follows:

$$\varphi_{i,j}=\arctan\frac{(y_{i,j}-x_{i,j+1})\cdot(x_{i,j}-x_{i+1,j})-(y_{i,j}-y_{i+1,j})\cdot(x_{i,j}-x_{i,j+1})}{(y_{i,j}-y_{i,j+1})\cdot(y_{i,j}-y_{i+1,j})+(x_{i,j}-x_{i+1,j})\cdot(x_{i,j}-x_{i,j+1})}. \tag{34}$$

According to the analysis presented above, the volume of the interference part is

$$\begin{cases} V_{i,j}=\dfrac{1}{3}\cdot S_{\mathrm{t}}^{(i)}\cdot h_{i,j}, \\ V_{i,j+1}=\dfrac{1}{3}\cdot S_{\mathrm{t}}^{(i)}\cdot h_{i,j+1}, \\ V_{i+1,j}=\dfrac{1}{3}\cdot S_{\mathrm{t}}^{(i)}\cdot h_{i+1,j}. \end{cases} \tag{35}$$

The volume of the three adjacent abrasive clearance spaces that can accommodate the lubricant can be expressed as

$$V_{\mathrm{s}}^{(i)}=V_{n}^{(i)}-V_{i,j}-V_{i,j+1}-V_{i+1,j}. \tag{36}$$

The number of clearance spaces N_{t} contained in all abrasive particles of the grinding zone is

$$N_{\mathrm{t}}=2\cdot(N_x-1)\cdot(N_y-1). \tag{37}$$

Therefore, the total volume of all abrasive clearance

spaces is

$$V_{\text{total}} = \sum_{1}^{N_t} V_s^{(i)}. \tag{38}$$

According to topography model, at a cutting depth of 30 μm, the contact arc length l_c is approximately 3 mm. The abrasive particles on the wheel surface will quickly change as it spins with great velocity. Therefore, the clearance volume V_{total} and total volume V_g of all the abrasive particles change dynamically with time, and the dynamic change law during one cycle of wheel rotation is shown in Fig. 15. The distribution domain of the abrasive clearance volume in the grinding zone is [70.46, 78.72] mm^3, and the distribution domain of the abrasive total volume is [140.84, 155.67] mm^3.

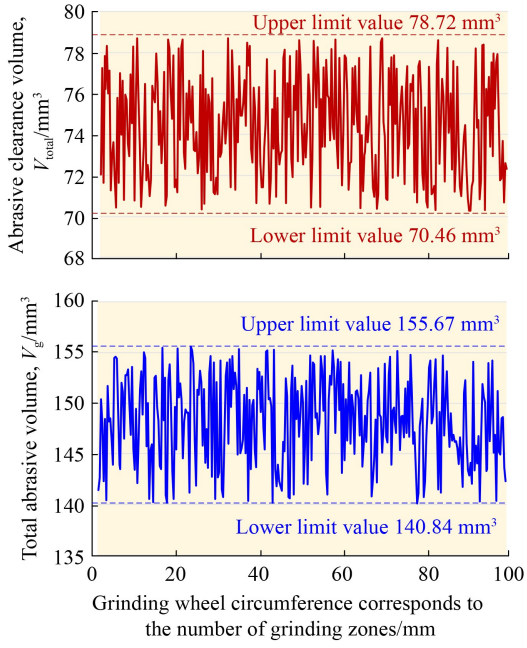

Fig. 15 Dynamic variations in grain total volume and space total volume.

In the exploration of the holding capacity of a lubricant by abrasive clearance, a comparison with the corresponding lubricant film volume V_f is required. Owing to the irregularity of thickness distribution, the average thickness h_{f_ave} can be analyzed to facilitate the calculation. The lubricant film volume V_f under different cryogenic air conditions is displayed in Table 2. The volume of the oil film V_f at various cryogenic air conditions is less than the lower limit value of the abrasive clearance volume V_{total}. Theoretically, during grinding, the lubricant cannot entirely fill the abrasive clearance. Therefore, under boundary lubrication conditions, effectively increasing h_f (in accordance with the volume of the nearby liquid film) will help to expand the capacity for oil storage in an abrasive gap, thereby improving lubrication capacity, effectively reducing grinding heat generation, and improving heat transfer capacity.

Table 2 Lubricant film volume under different cryogenic air conditions

Cryogenic air/°C	Average liquid film thickness, h_{f_ave}/mm	Liquid film volume, V_f/mm^3
−10	0.701	42.06
−20	0.825	49.50
−30	0.873	52.38
−40	0.953	57.18
−50	1.065	63.90

5 Grinding performance of CAMQL

Variations in cryogenic air temperature can change the thickness of a liquid film formed by atomized droplets on a workpiece surface and then affect the flow rate of the lubricant in the grinding zone. To further reflect the influence of lubricant flow on grinding performance, grinding performance experiments are carried out, using controlling variables. Only the cryogenic air temperature is used as a variable, and other parameters are set to constants. Grinding performance is characterized by grinding temperature, specific grinding force, friction coefficient, specific grinding energy, and workpiece surface quality.

5.1 Equipment and material

Titanium alloy is selected for the experiment. The model is Ti-6Al-4V with a size of 80 mm × 20 mm × 40 mm. The Ti-6Al-4V titanium alloy's physical characteristics are displayed in Table 3.

Table 3 Physical properties of Ti-6Al-4V

Parameter type	Value	Unit
Thermal conductivity	7.955	W/(m·K)
Specific heat	526.3	J/(kg·K)
Density	4.42	kg/m^3
Elasticity modulus	114	GPa
Poisson's ratio	0.342	–
Yield strength	880	MPa
Shearing strength	700	MPa
Rockwell hardness	35	GPa

Figure 16 displays the measuring tool and grinding system. A CBN grinding wheel with a size of 300 mm × 20 mm × 76.2 mm is adopted. To ensure efficient transport and prevent the lubricant from solidifying, a special micro lubricant F30-A with cryogenic resistance

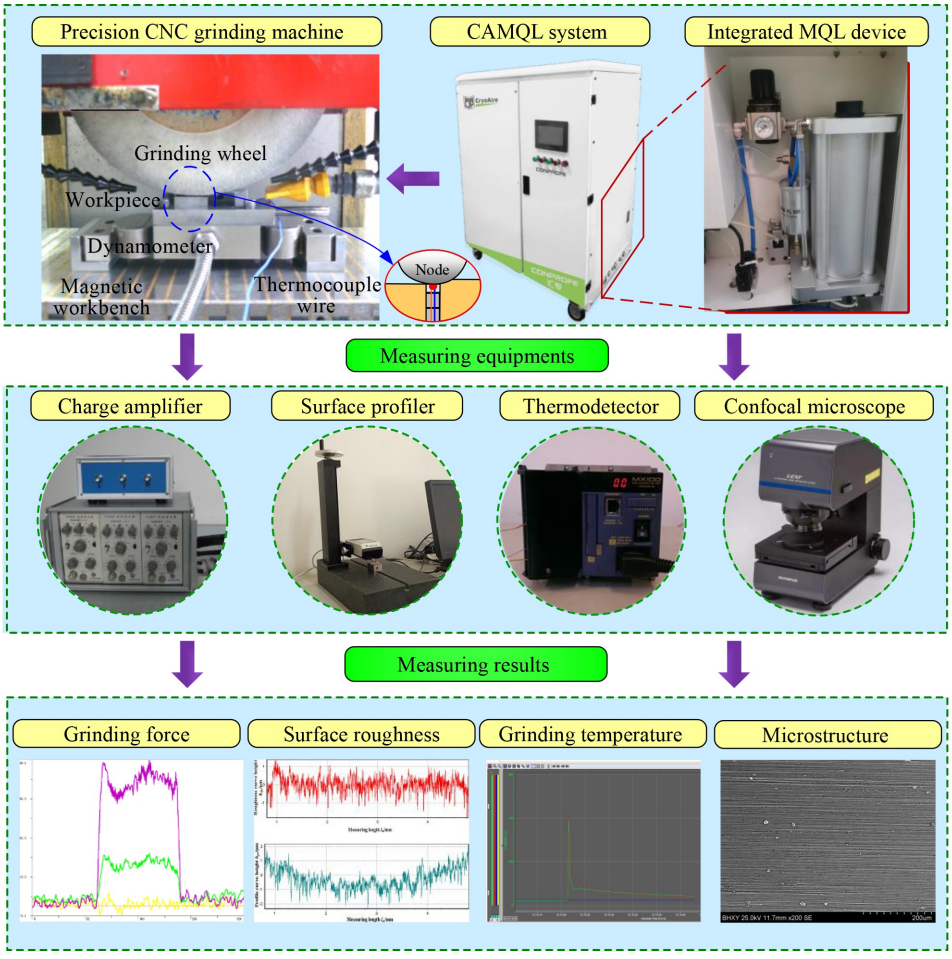

Fig. 16 Schematic of experimental measurement process.

is used. It is plant based and biodegradable and has a density of 850 kg/m^3 and freezing point of −20 °C.

The grinding force is measured with a YDM-III99 instrument, and temperature is measured using an MX100 thermocouple. A clip-on thermocouple is used to measure temperature in the grinding zone. After grinding, the workpiece is removed, and the surface roughness *Ra* is measured with a TIME 3220 surface profile instrument. The microscopic morphology of the machined workpiece surface is analyzed using an OLS-5000 laser confocal microscope. The experimental scheme is shown in Table 4.

Table 4 Grinding test parameters

Parameter	Value	Unit
Grinding type	Plane grinding	–
Grinding wheel type	CBN grinding wheel	–
Cooling type	CAMQL	–
Circular linear speed, v_s	30	m/s
Feeding rate, v_w	4	m/min
depth of grinding, a_p	30	μm
Liquid flowing rate	60	mL/h
Nozzle distance, d	12	mm
Nozzle angle, α	15	°
Air pressure, P	0.4	MPa
Air temperature	−50, −40, −30, −20, −10, 0, 10, and 20	°C

5.2 Experimental result

5.2.1 Grinding temperature

At fixed jet and grinding parameters, the 10 peak temperature curves of each cryogenic condition are collected for average processing. The variation trend of maximum temperature at various airflow temperatures is shown in Fig. 17. The temperature in the grinding zone shows a decreasing trend as air flow temperature decreases. The grinding zone temperature drops to 232.1 °C at an air flow temperature of −50 °C. At 20 °C ambient temperature, a decrease of 54.7% is observed. Theoretically, air flow above a liquid film is stable, and an atomized droplet driving effect will not change at a constant pressure. Oil film viscosity will increase when temperature drops. This increase will partially impede

flow speed and bolster the oil film's thickness. Therefore, lubricant consumption per unit time will increase in the wheel's effective area. The theory of boundary lubrication states that by covering micro-grooves effectively, oil with increased volume will serve as a lubricant. In addition, the temperature of cryogenic air and liquid film have a positive correlation. Resistance to high temperatures during the grinding zone's brief contact time increases with decreasing liquid film temperature. As a result, oxidation and desorption adhesion are effectively promoted, which makes the oil film thickness maintains a valid bearing status. Moreover, the high-viscosity and cryogenic oil film will efficiently lower the quantity of heat produced during grinding. Concurrently, heat transfer increases, and grinding temperature considerably decreases under a superposition effect.

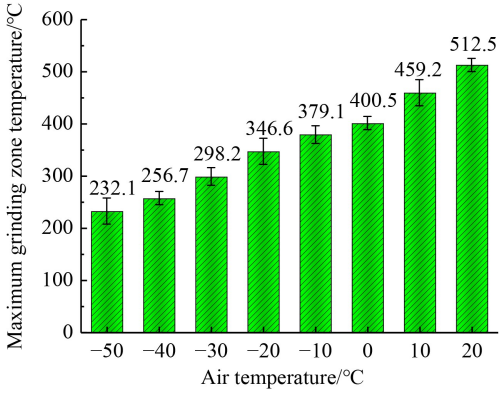

Fig. 17 Maximum temperature of the grinding zone at different air flow temperatures.

5.2.2 Specific grinding force and friction coefficient

Specific grinding force refers to the actual average load borne by wheel per unit width. Figure 18 indicates a decreasing trend of specific grinding force when air flow temperature decreases. When the air flow temperature is −50 °C, the specific tangential or normal forces obtained are the smallest, which are 2.43 and 2.55 N/mm, respectively. Relative to the room temperature (20 °C), temperature decreases by 53.6% and 52.5%. At room temperature, after the grinding wheel's entry into the grinding zone, the oil film lowers the grinding force while acting as a bearing and lubricant. However, elevated temperatures can easily lead to oil film rupture, and a high grinding force appears as a result. Cryogenic air flow can efficiently lower ambient temperature as air temperature drops, accelerating heat dissipation. Simultaneously, it aids in enhancing the heat transfer ratio. Additionally, it somewhat lowers a workpiece's surface temperature, which restrains adhesion to a grinding wheel, ultimately lowering grinding force. A low temperature causes the lubricant's viscosity to increase, and the oil film's thickness effectively lubricates and bears the contact area. Furthermore, the oil film maintains its high absorption and survival ability in the relatively cryogenic environment while preventing oxidation failure caused by high temperatures.

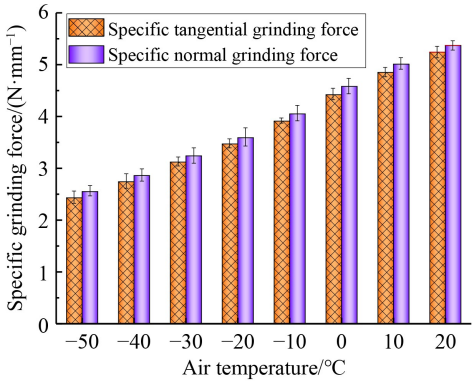

Fig. 18 Specific grinding force at different air flow temperatures.

An accurate way to describe the lubricating effect between sliding interfaces is to calculate friction coefficient, which is the ratio of F_t to F_n. The friction coefficient distribution of a grinding titanium alloy under different airflow temperature conditions is shown in Fig. 19. The specific grinding force decreases with airflow temperature. When the air flow temperature is −50 °C, the friction coefficient is the smallest (only 0.32). Relative to the friction coefficient at room temperature (20 °C), a decrease of 55.6% is observed. This result demonstrates that the friction coefficient can be effectively reduced by CAMQL, which in turn reduces the amount of friction heat generated.

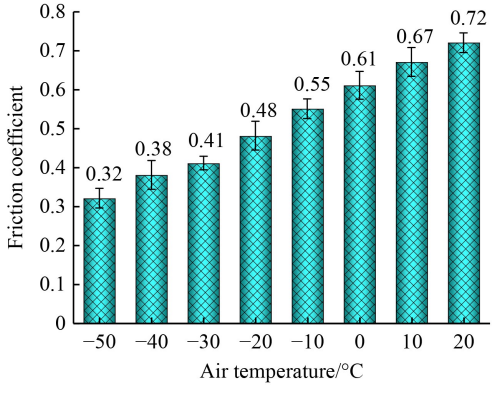

Fig. 19 Friction coefficient at different air flow temperatures.

5.2.3 Specific grinding energy

An essential grinding metric that can describe the lubricating impact of an interface is specific grinding

energy. Grinding performance improves with decreasing specific grinding energy, which is the energy for removing a given volume of material. A grinding performance's benefits and drawbacks can be determined by the degree of change in specific grinding energy that occurs as the cutting edge passivates [59–61].

For a specific grinding parameter, less energy is used when an identical workpiece material volume is removed because a small grinding force is generated. The effective grinding force is determined during the measurement process by averaging 20 grinding stroke data points. The energy expended during the entire grinding process is largely devoted to material removal, and heat is produced as a result of most energy conversion. Specific energy for various airflow temperature conditions is displayed in Fig. 20. Energy consumed by grinding increases with air flow temperature. When ambient temperature is 20 °C, the specific grinding energy is as high as 80.97 J/mm^3. Compared with −50 °C, airflow temperature increases by 47.3%. A low airflow temperature is conducive to lubricant cooling. After a film forms, it moves into the contact zone along with the wheel, thereby preventing the undesirable effects of evaporation, desorption, and oil film rupture and substantially lowering the likelihood of dry friction in the vicinity. A robust and adsorbent oil film can result in exceptional bearing performance. Moreover, grinding force can be effectively reduced when thickness and survival are guaranteed, and the flowing liquid film's convective, boiling heat transfer, and heat dissipation capacities improve. Abrasive chips' tendency to adhere to other abrasive particles through heat is partially inhibited, and thus grains retain their extraordinary machinability and sharpness over an extended period and exhibit enhanced capability to remove materials.

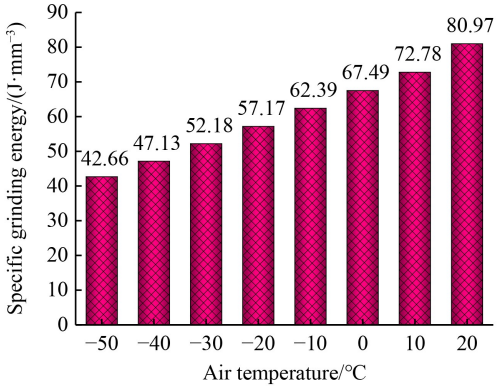

Fig. 20 Specific grinding energy under different conditions.

5.2.4 Workpiece surface quality

After the workpiece's grinding, it may have scratches, brittle plastic deformation, mechanical vibration, or other processing-related issues, which will inevitably lead to geometric errors. Thus, the workpiece has a certain surface roughness [32]. Micro-geometric features on a machined surface consisting of small peaks and valleys with small spacing are referred to as surface roughness, which is a key metric for assessing surface quality and is primarily determined by *Ra* and *RSm* [62–65].

The workpiece surface typical features under various airflow temperature conditions are captured using an OLS-5000 microscope, and workpiece surface quality is assessed, as illustrated in Fig. 21. With an adhesive recast layer that is nearly always covered in scaly patches and has a comparatively high number of adhesive points, the workpiece surface quality is the lowest at an airflow temperature of 20 °C. The reason for this is that grinding chips, when exposed to high temperatures and thermal softening conditions, easily bond to the wheel surface. They are unable to separate from the wheel in a timely manner and reattach to the workpiece's surface when the wheel makes rapid rotations, resulting in a scaly adhesion. Owing to the extensive adhesive layer, observing and distinguishing a parallel furrow group composed of abrasive particles are challenging. Inadequate cooling and lubrication result in the peeling of materials on the workpiece's surface. Practical grinding experience has shown that adhesive points increase with the distribution area of the adhesive recast layer. Grinding wheel clogging worsens, and grinding grain cutting performance is greatly reduced. As a result, surface roughness *Ra* and *RSm* of 0.78 and 0.082 μm are obtained, respectively.

The thickness of the liquid film increases somewhat as air flow temperature drops. Thus, the amount of lubricant used in a given amount of time will increase. Reduced grinding heat generation can be achieved through the use of high-viscosity oil films at low temperatures. The exchange of heat within the grinding zone increases, and grinding temperature is considerably reduced under the effect of superposition. Some improvements in the block spalling and flake adhesive recasting phenomena, good differentiation of the furrow group, and gradual reduction in adhesive points distribution range are observed. When air flow temperature is –50 °C, no evident adhesive recast layer forms. Differences between individual furrows width and depth are reduced, and a clear and nearly parallel group line appears in the furrow. Although the volume and amount of adhesion points greatly decrease and surface roughness is greatly enhanced, the points of adhesion remain intact possibly because the abrasive particles' notable heights protruding at different points. The *Ra* and *RSm* values decrease by 46.2% and 37.8%, respectively, relative to those at airflow temperature of 20 °C.

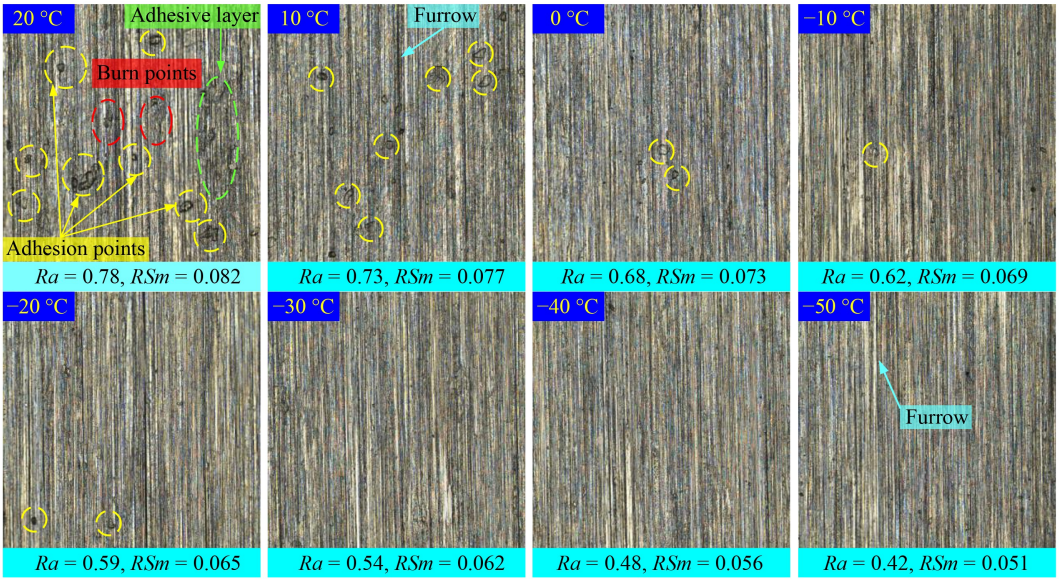

Fig. 21 Surface morphology of workpiece under different air temperatures. The units of *Ra* and *RSm* are μm.

6 Conclusions

A major factor in cooling and lubricating effects is liquid film state created by atomized droplets. The effect of nozzle position on liquid film distribution area is studied, and the film formation dynamic mechanism with CAMQL is analyzed. The process for determining a lubricant's effective flowing rate in a grinding zone is examined, the surface topography model based on a CBN wheel is created, and clearance volume distribution law is explored.

(1) The CAMQL low-temperature flowing liquid film is formed by the superimposed turbulent flow of airflow shear impact and steady flow of droplet impact. The movement behavior of atomized droplets after impacting a liquid film is calculated and analyzed. At a droplet group velocity of 12.24 m/s, a droplet group impact liquid film is spread and fuses without spatter. The boundary conditions of droplet impingement steady flow and air impingement-disturbed flow are analyzed by combining theory and simulation, and the normal and tangential momentum sources driving liquid film flow are obtained. Based on the mass/momentum continuity equation, the thickness distribution model of the flowing liquid film in the impact zone or non-impact zone is established. In the impact area, the liquid film thickness decreases first and then increases, and the liquid film thickness reaches the minimum value at the impact center. At the cryogenic air temperature of −10 to −50 °C, the liquid film thickness ranges from 0.92 to 1.26 mm. In the non-impact zone, the liquid film thickness is smaller than the liquid film edge thickness in the impact zone. At the cryogenic air temperature of −10 to −50 °C, the liquid film thickness ranges from 0.85 to 1.21 mm. The DIP method is used in measuring the thickness of the liquid film at different cryogenic air temperatures, and the experimental values are all smaller than the theoretical values.

(2) The surface topography model of the CBN grinding wheel is established on the basis of the random distribution of particle pose and spatial geometry. The geometric or morphological relationship of any three adjacent abrasive particles is analyzed, and the mathematical model of the abrasive clearance volume on the grinding surface of the grinding zone is established. During grinding, the distribution domain of the dynamic change of abrasive clearance volume is [70.46, 78.72] mm^3, and the total volume distribution domain of abrasive is [140.84, 155.67] mm^3. The relationship between the abrasive clearance volume and the corresponding oil film volume is further analyzed. Under the boundary lubrication condition, effectively increasing the liquid film thickness h_f will help to increase oil storage in the abrasive clearance and thus improve the lubrication capacity.

(3) The effects of different airflow temperature conditions on the grinding performance of titanium alloy materials are compared and analyzed. At fixed jet parameters and grinding parameters, reducing the air flow temperature contributes to the improvement in the grinding effect. When the air flow temperature is −50 °C, the grinding temperature, specific tangential grinding force, specific normal grinding force, friction coefficient, specific grinding energy, *Ra*, and *RSm* values are reduced by 54.7%, 53.6%, 52.5%, 55.6%, 47.3%, 46.2%, and 37.8%, respectively, relative to those at room temperature (20 °C).

Nomenclature

Abbreviations

CAMQL	Cryogenic air minimum quantity lubrication
CBN	Cubic boron nitride
DIP	Digital image projection

Variables

b_{wp}	Distance between half-stagnation point and stagnation point
C_f	Interface wave's phase velocity
d_p	Horizontal distance
D_d	Droplet size
D_n	Nozzle diameter
f_i	Interface shearing coefficient
F_n	Total normal force
F_t	Total tangential force
g_r	Unit mass force
h_f	Liquid film thickness
h_l	Liquid film thickness at nozzle
h_{f_ave}	Average liquid film thickness
K	Coefficient of determination
K_p	Constant parameter
l	Any side of projected triangle $\Delta A'B'C'$
L_a	Horizontal airflow thickness
L_n	Constant injection
m	Local mass flux of droplet
N_x	Number of radial abrasive particles
N_y	Number of axial abrasive particles
Oh	Ohnesorge number
p_s	Normal stress
P_{d_r}	Radial momentum source
P_{d_z}	Axial momentum source
P_{out}	Nozzle exit pressure
P_{out_a}	Air flow pressure
P_r	Momentum source
P_s	Pressure at stagnation poin
P_t	Half circumference of projected triangle $\Delta A'B'C'$
P_{total}	Air–liquid contact interface pressure
P_w	Pressure at position x
P'_w	Pressure in any position
P_{w_r}	Normal pressure of air flow on liquid film at any position
P_{w_z}	Tangential pressure of air flow on liquid film at any position
Q_f	Liquid film flow
R_p	Substrate size
Re_a	Airflow Reynolds number
s_p	Vertical distance
$S_{\Delta A'B'C'}$	Projected triangle's area
v'_a	Horizontal airflow velocity
v_d	Velocity droplet
v^*_d	Normal velocity
v_f	Kinematic viscosity
V_a	Air volume at the nozzle
V_f	Liquid film volume
V_g	Total volume
$V_s^{(i)}$	Space volume of three adjacent abrasive grains
V_{total}	Clearance volume
w	Wheel width
We	Weber number
α_d	Angle between droplet movement direction and vertical direction
σ_d	Tension coefficient of surface
σ_l	Tension coefficient of surface
β_p	Proportional coefficient
ρ_a	Air density
ρ_d	Droplet density
ρ_l	Liquid film density at the nozzle
ρ_f	Liquid film density
τ_f	Interfacial shearing stress
τ_{total}	Air–liquid contact interface shearing stress
τ_s	Surface shear stress
μ_d	Dynamic viscosity
μ_f	Dynamic viscosity
μ_l	Kinematic viscosity

Acknowledgements This study was financially supported by the National Natural Science Foundation of China (Grant No. 52375447), Shandong Provincial Natural Science Foundation of General Program, China (Grant No. ZR2024ME205), the Special Fund of Taishan Scholars Project, China (Grant No. tsqn202408220), and Shandong Provincial Natural Science Foundation of Youth Fund, China (Grant No. ZR2021QE116).

Conflict of Interest Changhe LI is a member of the Editorial Board of *Frontiers of Mechanical Engineering*, who was excluded from the peer review process and all editorial decisions related to the acceptance and publication of this article. Peer review was handled independently by the other editors to minimize bias.

References

1. Namlu R H, Lotfi B, Kiliç S E. Enhancing machining efficiency of Ti-6Al-4V through multi-axial ultrasonic vibration-assisted machining and hybrid nanofluid minimum quantity lubrication. Journal of Manufacturing Processes, 2024, 119: 348–371
2. Dang J Q, Zhang H, An Q L, Ming W W, Chen M. Surface modification of ultrahigh strength 300M steel under supercritical carbon dioxide (scCO2)-assisted grinding process. Journal of Manufacturing Processes, 2021, 61: 1–14
3. Liu M Z, Li C H, Yang M, Gao T, Wang X M, Cui X, Zhang Y B, Said Z, Sharma S. Mechanism and enhanced grindability of cryogenic air combined with biolubricant grinding titanium alloy. Tribology International, 2023, 187: 108704
4. Banerjee S, Ghosal S, Dutta T. Development of a simple technique for improving the efficacy of fluid flow through the grinding zone. Journal of Materials Processing Technology, 2008, 197(1–3): 306–313
5. Yang M, Ma H, Li Z H, Hao J C, Liu M Z, Cui X, Zhang Y B, Zhou Z M, Long Y Z, Li C H. Force model in electrostatic atomization minimum quantity lubrication milling GH4169 and performance evaluation. Frontiers of Mechanical Engineering, 2024, 19(4): 28
6. Martínez-Galván E, Ramos J C, Antón R, Khodabandeh R. Influence of surface roughness on a spray cooling system with R134a. Part II: film thickness measurements. Experimental Thermal and Fluid Science, 2013, 48: 73–80
7. Pautsch A G, Shedd T A. Adiabatic and diabatic measurements of the liquid film thickness during spray cooling with FC-72. International Journal of Heat and Mass Transfer, 2006, 49(15–16): 2610–2618
8. Wu H, Zhang F J, Zhang Z Y, Hou L. Atomization and droplet dynamics of a gas-liquid two-phase jet under different mass loading ratios. International Journal of Multiphase Flow, 2022, 151: 104043
9. Alekseenko S V, Bobylev A V, Evseev A R, Karsten V M, Markovich D M, Tarasov B V. Measurements of the liquid-film thickness by a fiber-optic probe. Instruments and Experimental Techniques, 2003, 46(2): 260–264
10. Muzik T, Safarik P, Tucek A. Analysis of the water film behavior and its breakup on profile using experimental and numerical methods. Journal of Thermal Science, 2014, 23(4): 325–331
11. Leng M Y, Chang S N, Ding L, Li X F. Thickness of water film driven by gas stream on horizontal plane. Acta Aeronautica et Astronautica Sinica, 2017, 38(2): 520696–520704
12. Leng M, Chang S, Wu H. Experimental investigation of shear-driven water film flows on horizontal metal plate. Experimental Thermal and Fluid Science, 2018, 94: 134–147
13. Cherdantsev A V, Hann D B, Azzopardi B J. Study of gas-sheared liquid film in horizontal rectangular duct using high-speed LIF technique: Three-dimensional wavy structure and its relation to liquid entrainment. International Journal of Multiphase Flow, 2014, 67: 52–64
14. Chang S N, Yu W D, Song M J, Leng M Y, Shi Q Y. Investigation on wavy characteristics of shear-driven water film using the planar laser induced fluorescence method. International Journal of Multiphase Flow, 2019, 118: 242–253
15. Zhang K, Wei T, Hu H. An experimental investigation on the surface water transport process over an airfoil by using a digital image projection technique. Experiments in Fluids, 2015, 56(9): 173
16. Liu Y, Zhang K, Tian W, Hu H. An experimental study to characterize the effects of initial ice roughness on the wind-driven water runback over an airfoil surface. International Journal of Multiphase Flow, 2020, 126: 103254
17. Singh G, Tiwari N. Thin film dynamics using lattice Boltzmann method: Role of aspect ratio and surface wettability gradient. Physics of Fluids, 2022, 34(7): 072104
18. Vinnichenko N A, Pushtaev A V, Plaksina Y Y, Uvarov A V. Performance of background oriented schlieren with different background patterns and image processing techniques. Experimental Thermal and Fluid Science, 2023, 147: 110934
19. Hu H, Wang B, Zhang K, Lohry W, Zhang S. Quantification of transient behavior of wind-driven surface droplet/rivulet flows using a digital fringe projection technique. Journal of Visualization, 2015, 18(4): 705–718
20. Xie J L, Zhao R, Duan F, Wong T N. Thin liquid film flow and heat transfer under spray impingement. Applied Thermal Engineering, 2012, 48: 342–348
21. Mantripragada V T, Sarkar S. Prediction of drop size from liquid film thickness during rotary disc atomization process. Chemical Engineering Science, 2017, 158: 227–233
22. Cheng W L, Han F Y, Liu Q N, Zhao R. Theoretical investigation on the mechanism of surface temperature non-uniformity formation in spray cooling. International Journal of Heat and Mass Transfer, 2012, 55(19–20): 5357–5366
23. Siavash Amoli B, Mousavi Ajarostaghi S S, Sedighi K, Aghajani Delavar M. Evaporative pre-cooling of a condenser airflow: investigation of nozzle cone angle, spray inclination angle and nozzle location. Energy Sources, Part A: Recovery Utilization and Environmental Effects, 2022, 44(3): 8040–8059
24. Gao T, Xu P M, Wang W, Zhang Y B, Xu W H, Wang Y Q, An Q L, Li C H. Force model of ultrasonic empowered minimum quantity lubrication grinding CFRP. International Journal of Mechanical Sciences, 2024, 280: 109522
25. Schmidt P, Ó Náraigh L, Lucquiaud M, Valluri P. Linear and nonlinear instability in vertical counter-current laminar gas-liquid flows. Physics of Fluids, 2016, 28(4): 042102
26. Martínez-Galván E, Ramos J C, Antón R, Khodabandeh R. Film thickness and heat transfer measurements in a spray cooling system with R134a. Journal of Electronic Packaging, 2011, 133(1): 011002
27. Liang G T, Zhang T Y, Chen Y, Chen L Z, Shen S Q. Two-phase heat transfer of multi-droplet impact on liquid film. International Journal of Heat and Mass Transfer, 2019, 139: 832–847
28. Rioboo R, Bauthier C, Conti J, Voué M, De Coninck J. Experimental investigation of splash and crown formation during single drop impact on wetted surfaces. Experiments in Fluids, 2003, 35(6): 648–652
29. Okawa T, Shiraishi T, Mori T. Production of secondary drops

during the single water drop impact onto a plane water surface. Experiments in Fluids, 2006, 41(6): 965–974
30. Deng Y C, Xing W J, Jin Y, Leng X Y, Sato K, Nishida K, Ogata Y, Raut S. Effect of mixing port length on internal flow and near-field jet characteristics of twin-fluid atomizers. Atomization and Spray, 2024, 34(8): 55–81
31. Zhao Y J, Markides C N, Matar O K, Hewitt G F. Disturbance wave development in two-phase gas-liquid upwards vertical annular flow. International Journal of Multiphase Flow, 2013, 55: 111–129
32. Guo Z F, Guo B, Wu G C, Xiang Y, Meng Q Y, Jia J F, Zhao Q L, Li K A, Zeng Z Q. Three-dimensional topography modelling and grinding performance evaluating of micro-structured CVD diamond grinding wheel. International Journal of Mechanical Sciences, 2023, 244: 108079
33. Liu M Z, Li C H, Jia D Z, Liu X, Zhang Y B, Yang M, Cui X, Gao T, Dambatta Y S, Li R Z. Model of atomized droplets average particle size and verification of eco-friendly hybrid lubrication (CAMQL). Friction, 2025 (in press)
34. Mohamed H, Biancofiore L. Linear stability analysis of evaporating falling liquid films. International Journal of Multiphase Flow, 2020, 130: 103354
35. Abbasi B, Kim J, Marshall A. Dynamic pressure based prediction of spray cooling heat transfer coefficients. International Journal of Multiphase Flow, 2010, 36(6): 491–502
36. Liu N, Yu Z X, Liang Y, Zhang H. Effects of mixed surfactants on heat transfer performance of pulsed spray cooling. International Journal of Heat and Mass Transfer, 2019, 144: 118593
37. Zhou Z F, Lin X W, Ji R J, Zhu D Q, Chen B, Wang H, Lu Y J. Enhancement of heat transfer on micro- and macro- structural surfaces in close-loop R410A flashing spray cooling system for heat dissipation of high-power electronics. Applied Thermal Engineering, 2023, 223: 119978
38. Baydar E, Ozmen Y. Investigation of thermal-flow behavior and droplet dynamics of mist sweeping impinging jet cooling. ASME Journal of Heat and mass transfer, 2023, 145(11): 113701
39. Pathan K A, Dabeer P S, Khan S A. Effect of nozzle pressure ratio and control jets location to control base pressure in suddenly expanded flows. Journal of Applied Fluid Mechanics, 2019, 12(4): 1127–1135
40. Charmiyan M, Azimian A R, Keirsbulck L, Shirani E, Aloui F. Turbulent plane impinging jet-physical insight and turbulence modeling. Journal of Applied Fluid Mechanics, 2016, 9(1): 11–17
41. Hu J G, Wang J X, Zhu C L, Zhu C X, Zhao N, Liu S Y. Experimental study on surface fluctuation characteristics of flat water film driven by airflow. Journal of Nanjing University of Aeronautics and Astronautics, 2022, 54(2): 259–266 (in Chinese)
42. Büttner L, Leithold C, Czarske J. Interferometric velocity measurements through a fluctuating gas-liquid interface employing adaptive optics. Optics Express, 2013, 21(25): 30653–30663
43. Setyawan A, Indarto, Deendarlianto. The effect of the fluid properties on the wave velocity and wave frequency of gas–liquid annular two-phase flow in a horizontal pipe. Experimental Thermal and Fluid Science, 2016, 71: 25–41
44. Zheng P, Zhao L. Correcting interface turbulence viscosity using CFD modeling for predicting stratified gas–liquid flow shear stress in horizontal pipes. European Journal of Mechanics-B/Fluids, 2020, 79: 202–211
45. Burgmann S, Krämer V, Rohde M, Dues M, Janoske U. Inner and outer flow of an adhering droplet in shear flow. International Journal of Multiphase Flow, 2022, 153: 104140
46. Chen M K, Zhang Y B, Liu B, Zhou Z M, Zhang N Q, Wang H H, Wang L Q. Design of intelligent and sustainable manufacturing production line for automobile wheel hub. Intelligent and Sustainable Manufacturing, 2024, 1(1): 10003
47. Wu J L, Ke X Z, Feng X R. Measurement of transverse wind speed in atmospheric turbulence by cross-correlation algorithm. Optical Engineering, 2022, 61(6): 066110
48. Dang J Q, Zhang H, An Q L, Ming W W, Chen M. On the microstructural evolution pattern of 300 M steel subjected to surface cryogenic grinding treatment. Journal of Manufacturing Processes, 2021, 68: 169–185
49. Li Q L, Ding K, Lei W N, Chen J J, He Q S, Chen Z Z. Investigation on induction brazing of profiled cBN wheel for grinding of Ti-6Al-4V. Chinese Journal of Aeronautics, 2021, 34(4): 132–139
50. Zhao B, Ding W F, Xiao G D, Zhao J S, Li Z. Self-sharpening property of porous metal-bonded aggregated cBN wheels during the grinding of Ti-6Al-4V alloys. Ceramics International, 2022, 48(2): 1715–1722
51. Ding W F, Zhao B, Zhang Q L, Fu Y C. Fabrication and wear characteristics of open-porous cBN abrasive wheels in grinding of Ti-6Al-4V alloys. Wear, 2021, 477: 203786
52. Zhang Y B, Gong P, Tang L Z, Cui X, Jia D Z, Gao T, Dambatta Y S, Li C H. Topography modeling of surface grinding based on random abrasives and performance evaluation. Chinese Journal of Mechanical Engineering, 2024, 37(1): 93
53. Wang J L, Zhang S H, Yang X, Peng F F. The influence of hard-brittle abrasive distribution on diamond cutting performance. Journal of Superhard Materials, 2021, 43(4): 285–295
54. Macerol N, Franca L F P, Krajnik P. Effect of the grit shape on the performance of vitrified-bonded CBN grinding wheel. Journal of Materials Processing Technology, 2020, 277: 116453
55. Kang M X, Zhang L, Tang W C. Study on three-dimensional topography modeling of the grinding wheel with image processing techniques. International Journal of Mechanical Sciences, 2020, 167: 105241
56. Liu M Z, Li C H, Zhang Y B, Yang M, Gao T, Cui X, Wang X M, Xu W H, Zhou Z M, Liu B, Said Z, Li R Z, Sharma S. Analysis of grinding mechanics and improved grinding force model based on randomized grain geometric characteristics. Chinese Journal of Aeronautics, 2023, 36(7): 160–193
57. Hu S G, Li C H, Li B K, Yang M, Wang X M, Gao T, Xu W H, Dambatta Y S , Zhou Z M, Xu P M. Digital twins enabling intelligent manufacturing: from methodology to application. Intelligent and Sustainable Manufacturing, 2024, 1(1): 10007
58. Si Q R, Lu R, Shen C H, Xia S J, Sheng G C, Yuan J P. An intelligent CFD-based optimization system for fluid machinery: automotive electronic pump case application. Applied Sciences, 2020, 10(1): 366
59. Song Y X, Li C H, Zhou Z M, Liu B, Sharma S, Dambatta Y S, Zhang Y B, Yang M, Gao T, Liu M Z, Cui X, Wang X M, Xu W

H, Li R Z, Wang D Z. Nanobiolubricant grinding: a comprehensive review. Advances in Manufacturing, 2025, 13: 1–42

60. Qu S S, Gong Y D, Yang Y Y, Wang W W, Liang C Y, Han B. An investigation of carbon nanofluid minimum quantity lubrication for grinding unidirectional carbon fibre-reinforced ceramic matrix composites. Journal of Cleaner Production, 2020, 249: 119353
61. Liu D W, Li C H, Xu P M, Wang W, Zhang Y B, Yang M, Cui X, Li B K, Liu M Z, Gao T, Dambatta Y S, Qin A G. Sicp/Al composites from conventional to empowered machining: Mechanisms and processability. Composite Structures, 2024, 346: 118433
62. Feng Z Q, Yi H A, Shu A H, Tang L. Simulation of grinding surface topography considering wheel wear and wheel vibration. The International Journal of Advanced Manufacturing Technology, 2024, 130(1–2): 475–490
63. Yang M, Hao J C, Wu W T, Li Z H, Ma Y Q, Zhou Z M, Gao T, Liu M Z, Cui X, Zhang Y B, Li B K, Ma X, Dambatta Y S, Li C H. Critical cutting thickness model considering subsurface damage of zirconia grinding and friction – wear performance evaluation applied in simulated oral environment. Tribology International, 2024, 198: 109881
64. Dambatta Y S, Li C H, Sayuti M, Sarhan A A D, Yang M, Li B K, Chu A X, Liu M Z, Zhang Y B, Said Z, Zhou Z M. Grindability evaluation of ultrasonic assisted grinding of silicon nitride ceramic using minimum quantity lubrication based SiO_2 nanofluid. Chinese Journal of Mechanical Engineering, 2024, 37(1): 25
65. Gu G Q, Wang D Z, Wu S J, Zhou S, Zhang B X. Research status and prospect of ultrasonic vibration and minimum quantity lubrication processing of nickel-based alloys. Intelligent and Sustainable Manufacturing, 2024, 1(1): 10006